國立交通大學

資 訊 科 學 系

博 士 論 文

心 臟 超 音 波 影 像 分 割 之 研 究

Study on Image Segmentation of Echocardiography

研 究 生：張純良

指導教授：荊宇泰　教授

中 華 民 國 九 十 三 年 七 月

心 臟 超 音 波 影 像 分 割 之 研 究

Study on Image Segmentation of Echocardiography

研 究 生：張純良

指導教授：荊宇泰　教授

國立交通大學

電機資訊學院

資訊科學研究所

博士論文

A Dissertation

Submitted to

Institute of Computer and Information Science

College of Electrical Engineering and Computer Sciemce

National Chiao Tung University

in Partial Fulfillment of the Requirements for

the Degree of Doctor of Philosophy

in

Computer and Information Science

July　2004

Hsinchu, Taiwan, Republic of China

中 華 民 國　九 十 三 年　七 月

心 臟 超 音 波 影 像 分 割 之 研 究

Study on Image Segmentation of Echocardiography

摘 要

我們提出兩種以區塊為主的影像分割方法及兩種以邊緣為主的影像分割方法，其中所提出的第一個以區塊為主的方法是乏析賀菲爾德(Hopfield)類神經網路，在這個方法中使用了全體的和區域性的影像亮度資訊來建構這個類神經網路，當網路趨於穩定狀態時，就可以獲得影像分割的結果；另一個提出的以區塊為主的方法是α形狀技術的分割方法，選擇了適當的α大小之後，每個區塊會對應到其中的一個分群中，再藉由和 AQ 的比對，就可以知道哪個分群是我們所要的心臟了。而所提出的第一個以邊緣為主的方法是使用圖形理論中尋找最短路徑的方法，我們先將影像以圓形的方向展開，並對應成一個有方向性的圖形，為避免落入小區域中的最佳值，我們使用了動態程式的方式找出最佳路徑；另一個以邊緣為主的方法是適合於物體形狀的邊緣不像圓形的影像分割，我們使用了α周線來建構尋找的範圍，並將其對應至有方向性的圖形中，同樣的用動態程式的方法尋找最佳路徑。

另外我們也提出了從心臟超音波影像中擷取心臟瓣模線的方法，在這個方法中需要一個專業醫生提供左心房內的一個點，結果的平均誤差是 3%，這在臨床上是可以接受的，這可以大大的節省醫生使用機器的時間，轉而將時間花在病人身上。

Study on Image Segmentation of Echocardiography

Student: Chwen-Liang Chang Advisor: Dr. Yu-Tai Ching

Institute of Computer and Information Science
College of Electrical Engineering and Computer Science
National Chiao Tung University

Abstract

In this dissertation, we propose two region-based segmentation algorithms and two edge-based segmentation algorithms for echocardiographic images. The first proposed algorithm of region-based segmentation scheme is fuzzy Hopfield neural network with fixed weight approach. This approach incorporated the global gray-level information and local gray-level information to construct a fuzzy Hopfield neural network. When the network converges to a stable state, the segmentation result will be obtained. A new approach using α-shape points is another proposed algorithm of region-based category. The region of interest corresponds to one of the clusters under a properly selected α. We identify the heart chamber in the ultrasound image by comparing the similarity between the α-connected components against the heart chamber obtained from the AQ image. The first proposed algorithm of edge-based segmentation scheme is finding the shortest path in directed graph. We circularly spread the image first and then map it to a directed graph. To avoid the local minimum trapping, dynamic programming approach is used for finding the shortest path. The other proposed approach for edge-based segmentation algorithm is suitable for non-circular like boundary. We incorporated an α-contour approach based on α-shape technique to construct the search

space and then map it to a directed graph. The dynamic programming technique also used for finding the shortest path.

In additional, we also propose a new approach for extracting mitral annular lines for echocardiographic images. A nearly automatic method for calculating the mitral annular lines from a 2D+1D precordial echocardiogram four-chamber view was presented. The proposed method needs only a physician to provide a point in the left ventricular chamber. The average error was 3% which is clinically acceptable. The proposed method saves much clinician time, allowing a shift from machine to patient care.

ACKNOWLEDGEMENTS

I would like to express my sincere appreciation to my advisor, Professor Yu-Tai Ching, for his kind patience and guidance throughout the course of this study. I also thank Professor Ling-Hwei Chen and Professor Cheng-Chung Lin, the menber of my proposal committee, for their valuable comments and constructive suggestions.

Many thanks are also given to the colleagues in the Medical Image Processing Laboratory of the Department of Computer and Information Science at National Chiao Tung University. Finally, I will dedicate this dissertation to my lovely families and my wife Ping-Ping Tseng for their endless love and constant concern during these years.

Contents

List of Figures

List of Tables

Chapter 1

Introduction

1.1 Research Motivation

According to American Heart Association statistics[3], cardiovascular disease has been the number one killer in the United States every year since 1900 but 1918. More than 2,600 Americans die of cardiovascular disease each day, an average of one death every 33 seconds. Cardiovascular disease claims almost as many lives each year as the next seven leading causes of death combined. Even the statistics of disease category is different between the U.S. and Taiwan, disease of heart is the third leading cause of death in the past years in Taiwan. According to the most recent computations of the Centers for Disease Control and Prevention of the National Center for Health Statistics (CDC/NCHS), if all forms of major cardiovascular disease were eliminated, life expectancy would rise by almost seven years. If all forms of cancer were eliminated, the gain would be three years. According to the same study, the probability at birth of eventually dying from major Cardiovascular diseases (ICD/9 390-448) is 47 percent, and the chance of dying from cancer is 22 percent. Additional probabilities are 3 percent for accidents, 2 percent for dia-betes and 0.7 percent for HIV.

Cardiac imaging is an established approach to diagnosis cardiovascular disease and play an important role in estimating the severity of various cardiac diseases. The possible methods of cardiac imaging are now published with X-ray computed tomography, magnetic resonance (MR), positron emission tomography, single photon emission computed tomography (SPECT),

and ultrasound. A detailed review of existing 3-D cardiac modeling approaches is provided in [28]. Cardiac ultrasound imaging (Echocardiography) is done in real time, making it more suitable for cardiology than other imaging modalities. It is preferable also because the equipment is portable, safe, and noninvasive.

Cardiac boundary extraction on echocardiographic images is essential for quantification of cardiac function. Among the various echocardiograms, the apical four-chamber view collected using a transthoracic transducer is important in evaluating the left ventricle function[2]. For example, the volume of the left ventricle can be estimated from the four-chamber image views. The left ventricle forces oxygen-rich blood into the arteries, which carry the blood throughout the body. The endocardial and epicardial boundaries of the Left Ventricle (LV) are useful quantitative measure for various cardiac functions such as left ventricle volume and ejection fraction. The basic quantitative measures of cardiac function will be introduced in Secion 1.3. In this task, left ventricle segmentation is the most important work. To segment the left ventricle, a physician can manually trace the boundary of the left ventricle in the images. This is a cumbersome and time-consuming job, especially when many images are involved. An automatic or semi-automatic method to segment the left ventricle would be a valuable diagnostic tool. Many reseachers have proposed some methods for echocardiographic image segmentation in the past years, such as [5, 7, 11, 33, 48, 60, 71, 81, 82]. This task is important but difficult. Echocardiographic image segmentation presents some challenging difficulty because of the inherent characteristics of the echocardiographic images, including blur, low contrast, speckle noise, and signal dropouts.

Image segmentation, a process to divide a given image into meaningful regions with homogeneous properties, is an essential step in image analysis and recognition. In general, image segmentation is based on gray level values. A great number of algorithms, for examples [1, 13, 14, 15, 29, 30, 32, 34, 43, 58, 64, 74, 83], have been proposed in the past. Those conventional image segmentation algorithms can be categorized generally into two classes:

1. Region-based schemes, by which homogeneous properties around a given pixel is enlarged.

2. Edge-based schemes, which detect the pixels with abrupt changes in gray levels, and then connect selected pixels to form completely enclosed boundaries.

In general, echocardiograpic image segmentation emphasizes the discrimination of regions associated with tissue and blood (cardiac cavities), making such structures easier to analyze. Besides the difficulties of the echocardiographic images segmentation, another problem occurs when the left ventricle is extracted from the segmented echocardiographic image. Mitral valve is one of the valves of the heart, whose function is to keep the blood flowing in one direction through the left atrium to the left ventricle, and to prevent backflow of blood when the heart contracts. Normally, the mitral valve opens when the heart relaxes, allowing blood to flow from the left upper chamber into the left lower chamber of the heart. However, in diastole the left ventricle and left atrium become one chamber when the mitral valve opens fully. This is the problem when we extract the left ventricles from the segmented results on echocardiographic images.

In this dissertation, we concertrate on a particular technique for ultrasound heart imaging, named as the four-chamber view. We focused our attention on the echocardiographic images segmentation. Two region-based algorithms and two edge-based algorithms are proposed for echocardiographic images segmentation. We also propose an approach for finding mitral annular lines from a sequence of echocardiographic images in order to separate the left ventricle and the left atrium of heart.

1.2 Nomenclature

n-D	n-dimensional.
AQ	Acoustic Quantitative.

CHNN	Competitive Hopfield neural network.
CI	Cardiac index.
CO	Cardiac output.
CT	Computed tomography.
CVD	Cardiovascular disease.
ECG	Echocardiography.
EDV	End diastolic volume.
EF	Ejection fraction.
ESV	End systolic volume.
FCM	Fuzzy c-means algorithm.
FHNN	Fuzzy Hopfield neural network.
HCM	Hard c-means algorithm.
HR	Heart Rate.
LoG	Laplacian of Gaussian
LV	Left ventricle.
LVV	Left ventricle volume.
MRI	Magnetic resonance imaging.
NN	Neural network.
ROI	Region of interest.
SPECT	Single photon emission computed tomography.
SV	Stroke volume.
SVI	Stroke volume index.
US	Ultrasound (imaging).

1.3 Basic parameters of cardiac function

In practice, the indices of the cardiac function are linked to the volumetric measures such as Left Ventricle Volume (LVV), Stroke Volume (SV), Ejection Fraction (EF), and Cardiac Output (CO) [12]. These basic parameters for the medical diagnosis are briefly described as follows.

LVV - *Left Ventricle Volume* is defined as the quantity of blood (ml) in the left ventricle. Angiocardiography and echocardiography have been traditionally used to assess this quantity. The achieved accuracy in the assessment of LVV with echocardiography varies largely with the model used to represent the LV. It has been shown that echocardiography consistently underestimates vertricular cavity, while angiocardiography consistently overestimates true volumes [77]. In summary the volume of the LV is a basic parameter required to obtain other LV indices, for example: EF.

SV - *Stroke Volume* is defined as the volume ejected between the end of diastole and the end of systole.

$$SV = EDV - ESV \tag{1.1}$$

EF - *Ejection Fraction* is a global index of LV fibers reduction, and is generally considered as one of the most meaningful measures of the LV pump function. It is defined as the ratio between the SV volume and the volume of the end of the diastole

$$EF = \frac{SV}{EDV} \times 100\% = \frac{EDV - ESV}{EDV} \times 100\%. \tag{1.2}$$

CO - *Cardiac Output* is defined as the product of the activity of pumping SV by the Heart Rate, HR.

$$CO = SV \times HR \tag{1.3}$$

The role of the heart is to deliver an adequate quantity of oxygenerated to the body. This blood flow is known as the cardiac output and is expressed in liters per minute. Since the

magnitude of CO is proportional to body surface, one person may be compared to another by means of the cardiac index, that is, the CO adjusted for body surface area.

1.4 Surveys of the Related Topics

In this section, we will introduce the surveys of the related topics of region-based and edge-based segmentation algorithms.

1.4.1 Region-based Image Segmentation

The principal approaches in region-based segmentation algorithms are based on thresholding, clustering, region growing, and region splitting and merging [30]. Region-based methods rely on the postulate that neighboring pixels within the one region have similar value. This leads to the class of algorithms known as region growing of which the "split and merge" technique [37] is probably the best known. The general procedure is to compare one pixel to its neighbors. If a criterion of homogeneity is satisfied, the pixel is said to belong to the same class as one or more of its neighbors. Adams and Bischof [1] proposed a method known as "Seeded Region Growing" which is based on the region growing postulate of similarity of pixels within regions. It is controlled by choosing a (usually small) number of pixels, known as seeds. Ikonomakis *et al.* [39] proposed a method known as "Region Growing and Region Merging" which start with a set of seed pixels and from these grows regions by appending the neighboring pixels that have similar properties. This process would be repeated until every pixel in the image would belong to a region. The merging procedure involves merging regions that are neighbors and which satisfy the homogeneity function with a new merging threshold M. A dynamic thresholding process was used in processing computerized tomography (CT) images for organ identification in [42]. The location, size, adjacency, and shape constraints of the organs were used as anatomical knowledge.

Recently, neural network based architectures [16, 17, 21, 23, 26, 47, 44, 45, 84] have been

applied for image segmentation. Dhawan and Arata [26] proposed a two-dimensional self-organizing feature map based approach, that incorporates both local and global information about the gray-level distribution of the image and explores the useful features of the image to determine and extract meaningful regions of interest. They used the concept of competitive learning to find the overall gray-level distribution of the image as the global information. A contrast measure defining the homogeneity of the region was also used as the local information. In [47][16] the image segmentation process was formulated as a constraint satisfaction problem (CSP) by interpreting it as a process of assigning labels to pixels. A three-dimensional constraint satisfaction neural network was developed to form the constraints in the CSP. A method using a competitive Hopfield neural network (CHNN), based upon the global gray-level values distribution, was proposed by Cheng *et al.* [17]. The problem of image segmentation is regarded there as minimization of a cost function, which, in turn, is defined as the mean value of distance measures between the gray-level values and the members of classes. Lin *et al.* [44] proposed a fuzzy Hopfield neural network (FHNN), based upon the pixel classification, for image segmentation. This approach added a fuzzy reasoning strategy into a neural network. In FHNN, the process of image segmentation is also regarded as a minimization problem in which the cost function is defined as the Euclidean distance between the gray levels in a histogram and the cluster centers represented in the gray levels. In general, those methods above for medical image segmentation make use of the local information, i.e. the gray-level values of the neighborhood pixels, and the global information, i.e. the overall gray-level distribution in the image.

1.4.2 Edge-based Image Segmentation

An edge is the boundary between two regions with relatively distinct gray-level properties. A typical boundary detection procedure in echocardiography studies has three steps [70], preprocessing by smoothing, enhancing, and identifying. Chu et al. [19] proposed an algo-

rithm based on the nonpurposive segmentation approach which consists of three steps, edge detecting, edge estimation, and nonlinearly edge processing. Coppini et al. [23] proposed an approach to extract left ventricle border including three step, edge detecting, edge grouping, and edge classification.

The most common method of edge detection in image segmentation application is the gradient. Some of earlier methods, such as the Roberts, Prewitt and Sobel operators [30], compute the gradient of an image based on obtaining the partial derivatives at every pixel location. These operators use local gradient operators to approximate the magnitude of the gradient for detecting the presence of an edge in an image. However, the Sobel operators have the advantage of providing both a differencing and a smoothing effect. Because derivatives enhance noise, the smoothing effect is a particularly attractive feature of the Sobel operators.

The famous Laplacian of Gaussian edge detection operator (LoG operator) proposed by D. Marr and E. Hildreth [51] smooths the image by using Gaussian distribution filter before convolving the image with Laplacian operator, and it extracts edges efficiently. The LoG operator is commonly employed as a second order edge detector in image processing, and is popular because of its attractive scaling properties. In the edge detection scheme the LoG operator is convolved with an image and the resulting zero crossings are classified as edges. Shen and Castan [68] used a symmetrical exponential filter in edge detection. However, since it was originally proposed by Marr and Hildreth, the Gaussian filter is by far the most widely used smoothing filter in edge detection [25, 63, 80]. A survey of Gaussian-based edge detection techniques may be found in [4].

Kass et al. [40] proposed the active contour model, known as Snake, to build a deformable contour which consists of connected spline segments and approximates to a desired form by minimizing an energy function which consist of internal, image, and constraint energy. The Snake model has been applied to medical image segmentation in variety of modalities. The Snake model needs an initial contour of border which is generally obtained by manual in-

put. Staib and Duncan [72] proposed an algorithm for boundary finding with probabilistic deformable models in order to increase the flexibility of enforcing the constraints in parameter space. In the case of boundary finding through the optimization in image space, the measure of fit is represented by certain image-related quantities. Suri et al. [75] proposed a methodology by which more accurate end-diastole and end-systole left ventricle boundaries can be automatically computed from the initial boundaries generated by a left ventricle pixel-based classifier. A formulation of the two-dimensional (2-D) deformable template matching problem is proposed in [76]. It uses a lower-dimensional search space than convertional methods by precomputing extensions of the deformable template along orthogonal curves. Ono and Ogawa [57] use the circularly spread image and a neural network to do segmentation in an MR image. They transformed the original image to a spread image. The segmentation task was converted to finding a polygonal line which divided the spread images to upper and lower halves. The polygonal line was determined by a neural network.

1.5 Organization of the Dissertation

This dissertation is composed of 6 chapters. The organization of the disertation is described as follows:

In Chapter 1, the motivation, nomenclature, basic parameters of cardiac function, surveys for the related topics, and organization of the dissertation are mentioned.

In Chapter 2, some traditional approaches of image segmentation are reviewed. In region-based schemes, we will introduce the hard c-means algorithm, fuzzy c-means algorithm, and competitive Hopfield neural network algorithm. In edge-based schemes, we will introduce the Sobel operator and the active contour model (Snake).

In Chapter 3, we will present the proposed fuzzy Hopfield neural network with fixed weight algorithm and the clustering algorithm using α-shape technique. These two algorithms are region-based.

In Chapter 4, we will propose two edge-based approaches using the shortest path finding algorithm for extracting the cadiac boundaries.

In Chapter 5, we will propose a new approach to find the mitral annular line from precordial echocardiogram using shortest path searching technique. The shortest path searching technique is also based on the proposed algorithm in chapter 4.

In Chapter 6, the dissertation is concluded and future works are stated.

Chapter 2

Reviews of the Methods for Image Segmentation

2.1 Introduction

As we stated in Section 1.1, segmentation algorithms are generally based on one of two basic properties of gray-level values: similarity and discontinuity. In the first category, the approach is to partition an image based on thresholding, region growing, and region splitting and merging. The principal approaches in the second category are based on abrupt changes in gray level.

In this chapter, we will review some region-based and edge-based segmentation algorithms. In region-based schemes, we will introduce hard c-means and fuzzy c-means, and Hopfield neural network schemes in Section 2.2 and 2.3, respectively. In edge-based schemes, we will introduce Sobel operator and active contour model in Section 2.4 and 2.5, respectively.

2.2 The Hard c-means and Fuzzy c-means Algorithms

The hard c-means and the fuzzy c-means algorithms are well known for classification of points in space into clusters. When these algorithms are applied for image segmentation, the pixels with similar intensity are gathered into clusters in order to identify the region of interest. In this section, these algorithms are briefly described for completeness. The details can be found in [6].

2.2.1 The Hard c-means Algorithm (HCM)

Given a set of n points denoted $X = \{x_1, x_2, \ldots, x_n\}$ in space. Suppose we divide the set of points into c clusters. It is said that the matrix $U = [u_{ik}] \in M_{nc}$ is a hard c-partition of X if it satisfies the following conditions:

$$\sum_{k=1}^{c} u_{ik} = 1,$$
$$\sum_{i=1}^{n} u_{ik} < n, \quad \text{and}$$
$$\sum_{i=1}^{n}\sum_{k=1}^{c} u_{ik} = n,$$

where $u_{ik} \in \{0, 1\}$.

The procedure of the hard c-means algorithm is summarized in the following steps.

1) Choose a primary set of c points, $\{v_k | k = 1, 2, \ldots, c\}$, as the cluster centers.

2) Calculate the membership matrix U based upon the minimum Euclidean distance as follows:

$$u_{ik} = \begin{cases} 1, & \text{if } (||x_i - v_k||)^2 = \min_{j=1}^{c}\{(||x_i - v_j||)^2\} \\ 0, & \text{otherwise} \end{cases}, \text{ for all } i, k.$$

3) Update the new cluster centers $\hat{v}_k$,

$$\hat{v}_k = \frac{\sum_{i=1}^{n}(u_{ik})(x_i)}{\sum_{i=1}^{n} u_{ik}}.$$

4) If $\hat{U} = U$ then stop; otherwise goto step 2).

The hard c-means algorithm is easy to implement. But it is sensitive to the noise in the image.

2.2.2 The fuzzy c-means algorithm (FCM)

The hard c-means algorithm allows a point to belong to only one cluster. But in the fuzzy c-means algorithm, every point belongs to all clusters with different degrees of the membership functions. The conditions of the membership matrix U of fuzzy c-means are modified as follows:

$$\sum_{k=1}^{c} u_{ik} = 1, \quad 1 \le i \le n,$$
$$\sum_{i=1}^{n} u_{ik} < n, \quad 1 \le k \le c, \quad \text{and}$$
$$\sum_{i=1}^{n}\sum_{k=1}^{c} u_{ik} = n,$$

where $0 \le u_{ik} \le 1$.

The procedure of the fuzzy c-means algorithm is summarized in the following steps.

1) Choose a set of points, $\{v_k | k = 1, 2, \ldots, c\}$, as the initial cluster centers.

2) Calculate membership matrix U for all points to all clusters using the following equation.

$$u_{ik} = \frac{\left[||x_i - v_k||^{-2}\right]^{\frac{1}{q-1}}}{\sum_{j=1}^{c}\left[||x_i - v_j||^{-2}\right]^{\frac{1}{q-1}}}.$$

3) Update the new cluster centers $\hat{v}_k$,

$$\hat{v}_k = \frac{\sum_{i=1}^{n}(u_{ik})^q x_i}{\sum_{i=1}^{n}(u_{ik})^q}.$$

4) If $\max_{ik} |\hat{u}_{ik} - u_{ik}| < \epsilon$, where ϵ is a stop criterion, then we stop the iteration. Otherwise the iteration restarts at step 2).

The fuzzification factor, q, a given real number which is greater than 1, decides the convergence speed and the sensitivity to noise. If q is set to 1^+, then it converges quickly and is less sensitive to the noise. On the other hand, if q is set to a large number, it will converge slowly and will be more sensitive to the noise.

2.3 Competitive Hopfield Neural Network

The Hopfield neural network, constructed with a feedback network, which needs many iterations before retriving a final pattern. It has the following characteristics:

1. Synaptic weights (predetermined by an energy function) are prestored.
2. Nonlinear thresholding operations are used in each stage to produce binary-valued states.
3. State feedbacks are used so that the states can be iteratively updated.
4. Iterations will converge to a solution that minimizes an energy function pertaining to the network.

In the following, a Hopfield network model will be introduced.

Given M binary-valued (0/1) patterns (i.e., $\{a_i^{(m)}\}$ have binary values 0 or 1), the weights of the Hopfield network are derived as

$$w_{ij} = \begin{cases} \sum_{m=1}^{M}(2a_i^{(m)} - 1)(2a_j^{(m)}), & i \neq j, \\ 0, & i = j. \end{cases} \tag{2.1}$$

The thresholds of the network are given as

$$\theta_i = -\frac{1}{2}\sum_{j=1}^{N} w_{ij}. \tag{2.2}$$

Let a_i denote the binary state of the ith neuron and w_{ij} be the interconnection weight determined in Equation (2.1) and (2.2) between the ith neuron and the jth neuron. A neuron i in this network would receive the inputs weighted by w_{ij} from every other neuron j may be calculated as

$$Net_i = \sum_{j \neq i} w_{ij}a_j + I_i. \tag{2.3}$$

The energy function (or Liapunov function) of the Hopfield network is given as follows:

$$E = -\frac{1}{2}\sum_i \sum_j w_{ij}a_i a_j - \sum_i I_i a_i. \tag{2.4}$$

The iterative Hopfield network model is summarized as follows:

Step 1) Compute the net value

$$Net(k+1) = \sum_j w_{ij} a_j(k) + \theta_i. \tag{2.5}$$

Step 2) Update the state

$$a_i(k+1) = \begin{cases} 1, & Net_i(k+1) > 0, \\ 0, & Net_i(k+1) < 0, \\ a_i(k), & Net_i(k+1) = 0. \end{cases} \tag{2.6}$$

Repeat the same process for the next iteration until convergence, which occurs when none of the elements changes state during any iteration.

2.4 Sobel Operator

The gradient is the most common method of differentiation in image processing applications. Dericatives may be implemented in digital form in serveral ways. However, the Sobel opertors have the advantage of providing both a differencing and a smoothing effect. For a function $f(x, y)$, the gradient of f at coordinates (x, y) is defined as the vector

$$\nabla \mathbf{f} = \begin{bmatrix} \frac{\partial f}{\partial x} \\ \\ \frac{\partial f}{\partial y} \end{bmatrix}. \tag{2.7}$$

The magnitude of this vector is defined as

$$\nabla f = mag(\nabla \mathbf{f}) = \left[\left(\frac{\partial f}{\partial x} \right)^2 + \left(\frac{\partial f}{\partial y} \right)^2 \right]^{\frac{1}{2}}. \tag{2.8}$$

The magnitude can be approximated by some of ways. The Sobel operator is one of the common used methods. Figure 2.1 shows a 3×3 region of an image, where the z's denote the values of intensity. The magnitude of gradient at point z_5 can be approximated by Sobel operator, written as

$$\nabla f \approx |(z_7 + 2z_8 + z_9) - (z_1 + 2z_2 + z_3)| + |(z_3 + 2z_6 + z_9) - (z_1 + 2z_4 + z_7)|. \tag{2.9}$$

z_1	z_2	z_3
z_4	z_5	z_6
z_7	z_8	z_9

Figure 2.1: A 3×3 region of an image, where the z's denote the values of intensity.

Computation of the gradient at the location of the center of the masks which gives one value of the gradient. To get the next value, the masks are moved to the next pixel location and the procedure is repeated. Thus, after the procedure has been completed for all possible locations, the result is a gradient image of the same size as the original image. As usual, mask operations on the border of an image are implemented by using the approapriate partial neighborhoods.

2.5 Active Contour Model

Active contour models were first proposed by Kass *et al.*[40]. This semiautomated image segmentation technique takes a rough user input on the location of an object and refines the object outline based on the computer-generated edge map. The active contour (snake) v is defined as a continuous deformable curve

$$v(s) = (x(s), y(s)),$$

where s denotes the normalized contour length. An energy that is a function of the contour's shape and position is associated with the snake. The optimal contour configuration is defined as one having the minimum energy. In general, the energy function consists of the internal and the external energy

$$E_{snake} = (E_{int}(v(s)) + E_{img}(v(s))ds.$$

E_{int} represents the internal energy that makes the contour resistant to bending and stretching, and E_{img} is the energy associated with the image that focus the contour to lock onto the edges. Since the position and shape of the snake are modified by the energy minimization process,

the lowest values of E_{img} should be at the locations where the image gradient is large, i.e., edge locations. Image energe is, therefore, often defined as

$$E_{img} = -||\Delta I||,$$

where I is the image intensity. The continuity and smoothness of the model help overcome the problems of gaps and noise in the object boundaries. Various approachs have been proposed for finding the optimal contour.

Chapter 3

Region Based Approach

3.1 Introduction

In this chapter, we will propose two region-based algorithms. As we mentioned, image segmentation refers to partitioning an image into different regions that are homogeneous or similar in some image characteristics. Region-based approaches which grow a region around a given pixel with homogeneous properties. Some related approaches are introduced in the previous two chapters. Generally speaking, these approaches make use of the local information, i.e. the gray-level values of the neighborhood pixels, and the global information, i.e. the overall gray-level distribution in the image, for image segmentation. The grobal information based methods are depended on the postulate that all pixels whose value (gray level, color value, or other) lie within a certain range belong to one class. This leads to the class of algorithms known as thresholding which is probably the best known. Such approaches neglect all of the spatial information of the image and do not cope well with noise or blurring at boundaries. The local information based methods rely on the postulate that neighboring pixels within the one region have similar value. The general procedure is to compare one pixel to its neighbors. If a criterion of homogeneity is satisfied, the pixel is said to belong to the same class as one or more of its neighbors. The choice of the homogeneity criterion is critical and the results are upset by noise.

The remainder of this chapter is organized as follows. In Section 3.2, the proposed fuzzy

Hopfield neural network with fixed-weight algorithm is presented. The proposed clustering algorithm using α-shape technique is presented in Section 3.3. In the last section, concluding remarks are included.

3.2 Fuzzy Hopfield Neural Network with Fixed Weight

In this proposed algorithm, we focus on noisy image segmentation. Due to the presence of noise, during region growing process the region of interest doesn't include the noisy pixels. Therefore, we propose a segmentation algorithm which incorporates both local and global information for medical image segmentation. The global gray-level information is used to segment the image for the initial partition. We then use local information to construct a Hopfield neural network. The Hopfield neural network simulates the membership function. The fuzzy set approach is applied to determine the outputs of the neurons. Each neuron corresponds to a pixel in the image. A pair of neurons are connected if they are neighbors in the image and the synaptic connection weights are predetermined and fixed to improve the efficiency. When the network converges into a stable state, a defuzzification process will decide to which cluster a pixel belongs and obtain the segmentation result.

3.2.1 Proposed Method

In this section, we present the proposed fuzzy Hopfield neural network with fixed weight model to simulate the membership matrix for image segmentation. Each pixel in the image is a point in the plane. If there are n pixels, to be divided into c clusters, then each pixel has c neurons associated with it. There are $n \times c$ neurons in this network. Similar to that in FCM, the outputs of the neurons, denoted $O = o_{ik}, 0 \leq i \leq n, 1 \leq k \leq c$, form a membership matrix. A membership corresponds to a partition if it satisfies the following conditions:

$$\sum_{k=1}^{c} o_{ik} = 1, \quad \text{for all } i,$$

$$\sum_{i=1}^{n} o_{ik} < n \quad \text{for all } k, \text{ and}$$
$$\sum_{i=1}^{n}\sum_{k=1}^{c} o_{ik} = n, \tag{3.1}$$

where $0 \leq o_{ik} \leq 1$. Two neurons are neighbors to each other if their corresponding pixels in the image are neighbors to each other. As shown in Figure 3.1, each neuron receives contributions from the neighboring neurons and itself as its input. These contributions are weighted by the synaptic weights, W. In our approach the synaptic weights are fixed and should be determined first. The synaptic weight between two neurons i and j is determined by the Euclidean distance and the similarity of their intensities in the image as shown in the following equation.

$$w_{ij} = \begin{cases} \frac{1}{\alpha_1(\Delta I(i,j))^2 + \alpha_2(D(i,j))^2}, & i \neq j, \\ 1, & i = j, \end{cases} \tag{3.2}$$

where $\Delta I(i,j)$ is the difference in intensity between pixel i and j, and $D(i,j)$ is the Euclidean distance between pixel i and j. α_1 and α_2 are the weights to balance these two factors.

The proposed method requires a set of initial cluster centers. The initial cluster centers can be obtained by analyzing the histogram of gray scales or our understanding of the images. In most of the cases in medical image segmentation, we know the intensities of the area of interest. When we acquire the c initial class centers, we can perform the initial partition as:

$$o_{ik}^{(0)} = \frac{\left(\frac{1}{(I(i)-v_k)^2}\right)^{\frac{1}{q-1}}}{\sum_{j=1}^{c}\left(\frac{1}{(I(i)-v_j)^2}\right)^{\frac{1}{q-1}}}, \quad 1 \leq i \leq n, 1 \leq k \leq c,$$

where $I(i)$ and v_k are respectively the intensity values of pixel i and the kth class center.

Recall that, a neuron receives outputs from neighboring neurons and itself. The net value of the neuron i is described as

$$\text{Net}_{ik}^{(t+1)} = \sum_{j \in N_i} w_{ij} o_{jk}^{(t)} + \theta_i \tag{3.3}$$

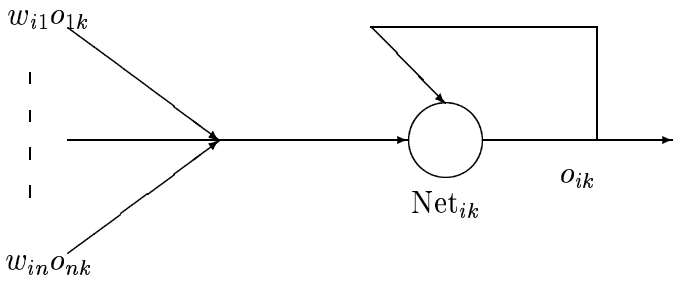

Figure 3.1: The structure of a neuron.

where $\text{Net}_{ik}^{(t+1)}$ is the net value of neuron i associated with class k in iteration $t+1$, $o_{jk}^{(t)}$ is the output state of neuron j associated with class k in iteration t, and θ_i is the offset bias fed to the neuron i. In our approach, the θ of all neurons are set to zero. So Equation (3.3) becomes

$$\text{Net}_{ik}^{(t+1)} = \sum_j w_{ij} o_{jk}^{(t)}. \tag{3.4}$$

Each pixel has c neurons associated with c clusters to represent the membership degree of each cluster. When the net values of the neurons have been updated in Equation (3.4), the outputs of all neurons will be updated depending on the new net values. Following the fuzzy c-means algorithm, the new output values can be obtained using the following equation:

$$o_{ik}^{(t+1)} = \frac{(\text{Net}_{ik}^{(t+1)})^{\frac{1}{q-1}}}{\sum_{j=1}^{c}(\text{Net}_{ij}^{(t+1)})^{\frac{1}{q-1}}}. \tag{3.5}$$

The proposed segmentation algorithm is summarized as follows:

Step 1) Determine the neighborhood window, N, and Calculate the weights,

$w_{ij}, \quad 1 \le i \le n, \quad$ for a neuron $j \in N_i$

using Equation (3.2).

Step 2) Initial clustering.

Step 3) Calculate the Net value using Equation (3.4).

Step 4) Update the output states using Equation (3.5).

Step 5) If $\max_{ik} \left| o_{ik}^{(t+1)} - o_{ik}^{(t)} \right| < \epsilon$ then goto Step 6);

otherwise $t = t + 1$ and goto Step 3).

Step 6) Output the final result using the defuzzification process as

$$S_i = k, \quad \text{if } o_{ik} = \max_{1 \le j \le c} \{o_{ij}\};$$

where S_i is the segmentation label of pixel i.

3.2.2 Simulation and Experimental Results

In this section, we present the experimental results. In our experiments, we used a set of phantom data and medical images to evaluate the performance of the proposed algorithm. The experiment used a phantom data set which was based on CHNN [17]. The phantom data is as shown in Figure 3.2(a), which was produced by four overlapping disks and the background. Each region had an average gray scale, as in the following

- the average gray value of the background was 30,
- from the outer most circle to the center, the average gray values of four disks were 75, 120, 165, and 210, respectively.

The gray scale in each region was not a constant. Suppose that μ is the average gray scale in a region. The gray scales in the region were uniformly distributed over the range $[\mu - K, \mu + K]$ where K is a constant. Figure 3.2(b)–(d) are the phantom data sets containing noise with K= 20, 23, 25, respectively. We applied the hard c-means (HCM), fuzzy c-means (FCM), competitive Hopfield neural network (CHNN), and the proposed approach to process the phantom data sets. Figures 3.3–3.5 are the segmentation results with noise levels K= 20, 23, and 25, respectively. In these figures, (a)–(d) are the results segmented by applying HCM, FCM, CHNN, and proposed approach, respectively. We compared the number of misclassified pixels and the error rates to evaluate the performance. Tables 1–3 show the comparison results from these phantom data sets using these four methods. All of the four methods perfectly segmented the objects when the noise level was K=20. If the noise levels were higher, when

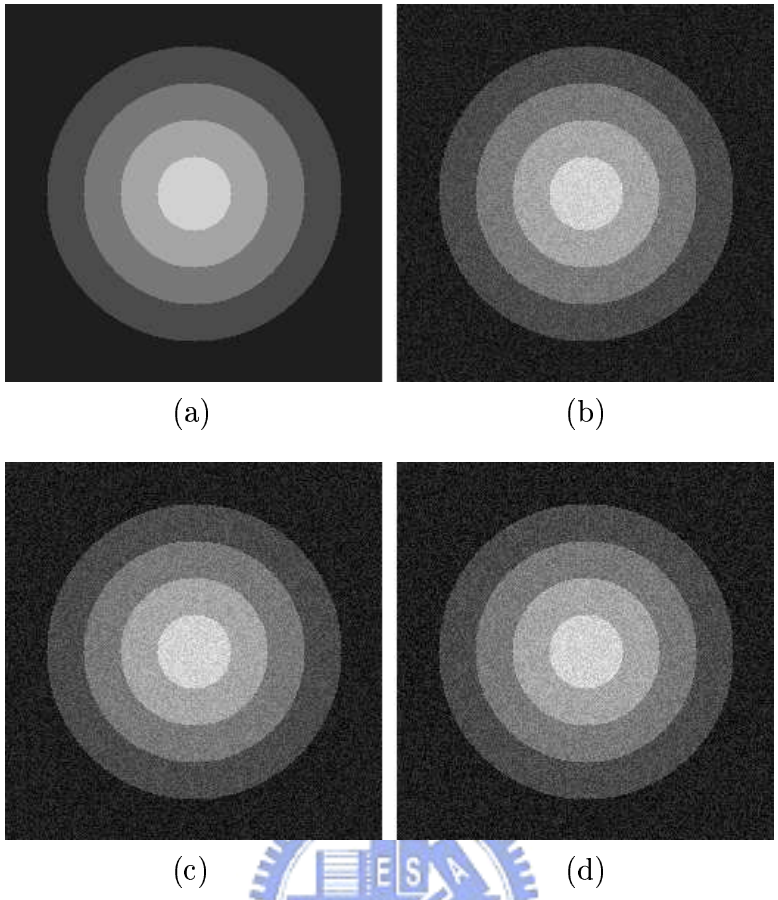

Figure 3.2: (a) The simulated image with a constant gray level in background and each disk. (b), (c), and (d) are the simulated images with added noise levels $K = 20$, 23, 25, respectively.

K=23 and 25, the performance of the proposed approach was better than other three methods, both in perception quality and quantitative comparisons (see Figure 3.4, 3.5 and Table 2, 3).

We applied the proposed algorithm to segment the area of interest in medical images. The first was a set of CT images of head scan. The region of interest in the CT images is a blood clot. The blood clot has higher intensity than the soft tissue. Two experiments were done on this set of images. The first experiment was to compare the proposed method against an intensity thresholding method. When we are partitioning the pixels into two classes, the effect of the proposed method is the same as the intensity thresholding method. The proposed method needs two initial cluster centers while the thresholding method needs an exact threshold value. When the thresholding method was applied, we first applied a mean

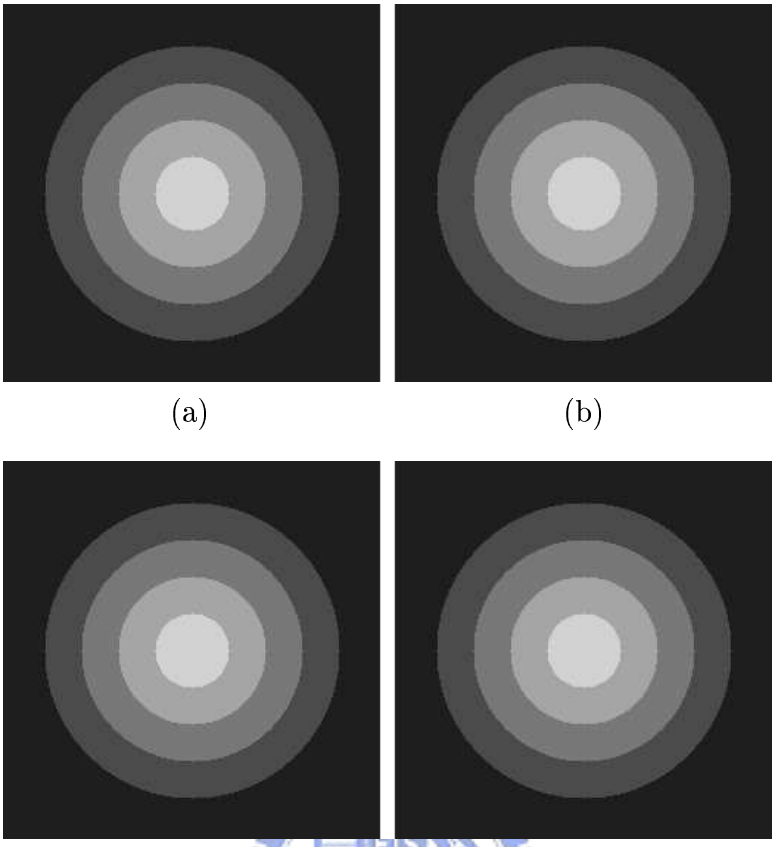

(a) (b)

(c) (d)

Figure 3.3: (a), (b), (c), and (d) are the segmentation results with added noise level $K = 20$ using HCM, FCM, CHNN, and proposed approach, respectively.

Table 3.1: The number of misclassified pixels and error rate with noise level K=20

	HCM	FCM	CHNN	proposed approach
Number of misclassified pixels	0	0	0	0
Error rate	0.00	0.00	0.00	0.00

Table 3.2: The number of misclassified pixels and error rate with noise level K=23

	HCM	FCM	CHNN	proposed approach
Number of misclassified pixels	31614	5090	9434	59
Error rate	0.4823	0.0776	0.1439	0.0009

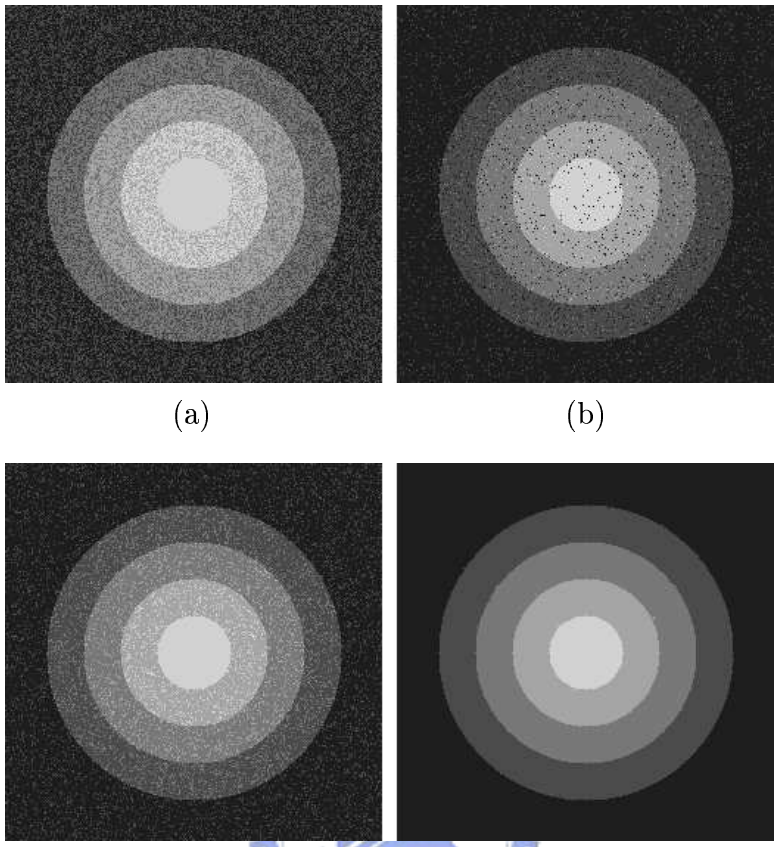

Figure 3.4: (a), (b), (c), and (d) are the segmentation results with added noise level $K = 23$ using HCM, FCM, CHNN, and proposed approach, respectively.

Table 3.3: The number of misclassified pixels and error rate with noise level K=25

	HCM	FCM	CHNN	proposed approach
Number of misclassified pixels	31644	8898	14022	361
Error rate	0.4828	0.1357	0.2139	0.0055

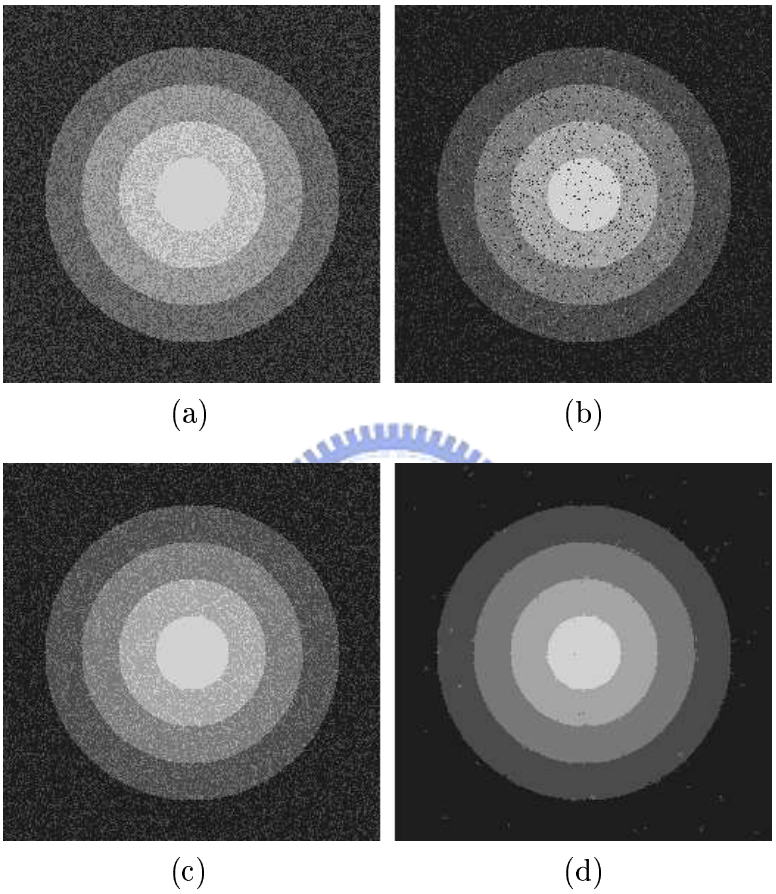

Figure 3.5: (a), (b), (c), and (d) are the segmentation results with added noise level $K = 25$ using HCM, FCM, CHNN, and proposed approach, respectively.

filtering to the image. We then carefully choosed the best possible threshold to segment the blood clot. The results are shown in Figure 3.6. In Figure 3.6, the first column shows the original image. The boundary points obtained by using the thresholding method are shown in the second column. The boundary points obtained by using the proposed method are shown in the third column. The proposed method can obtain relatively clean images.

The second experiment was to compare the proposed method with the HCM and FCM. Figure 3.7(a) is an original CT image of a human head scan. Figure 3.7(b) shows the blood clot segmented using the proposed approach. We also segmented the blood clot by using HCM and FCM algorithms and show the results in Figure 3.7 (c) and (d). The result obtained by the proposed approach was much better than the other two methods.

We applied the proposed method to classify the pixels in the echocardiographic images. In our experiment, precordial echocardiographic images were used. The region of interest in the echocardiographic images is generally the heart chamber. Heart chamber in the image generally has low intensity. The segmentation of a heart chamber is difficult due to the speckle noise. The boundaries of the segmented results from the proposed approach are shown together with the original images in Figure 3.8. These results show that the proposed approach works well for cardiac ultrasound images.

The next experiment was to classify the pixels in MR images of human head scan. We classified the pixels into four sets. Figure 3.9 shows the original images in the first row and the processed images in the second rows. The results show that the proposed method also works well to classify the pixels in MR images.

The proposed approach requires a set of initial cluster centers of gray scales. In the above experiments, the cluster centers were obtained by our scanning of the gray scales of the regions of interesting. It is not convenient for clinical applications. In this experiment, we provide an automatical technique to obtain the initial cluster centers by using the histogram of the image with global gray level information. The histogram of a digital image is a discrete function

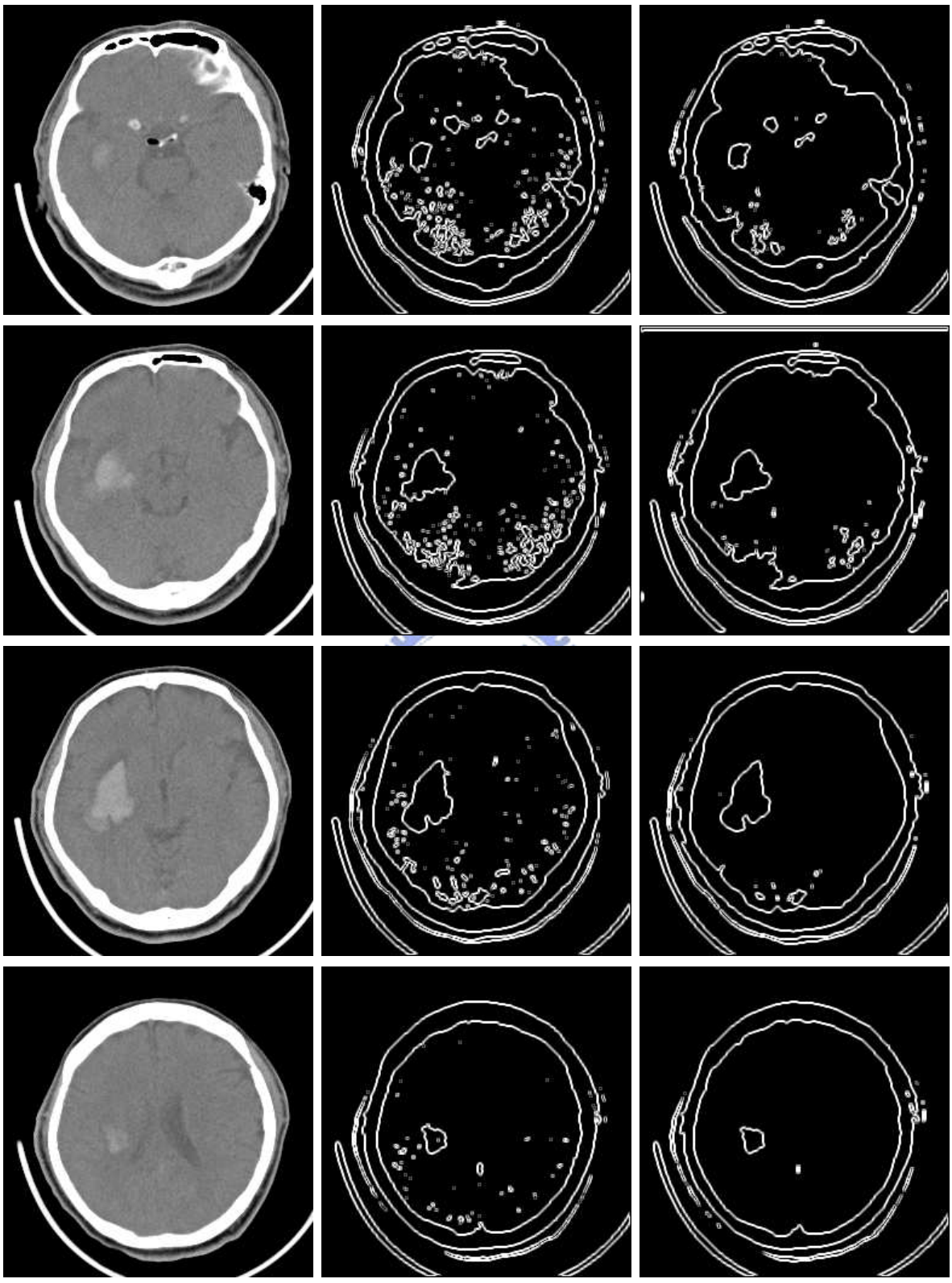

Figure 3.6: We partitioned the pixels in the CT images into 2 sets. We then calculated the boundaries for the pixels in the same set. The images in the first column are the original images. Images in the second column were obtained by first applying mean filter to the original images then applying intensity thresholding. The images in the third column were obtained by the proposed method.

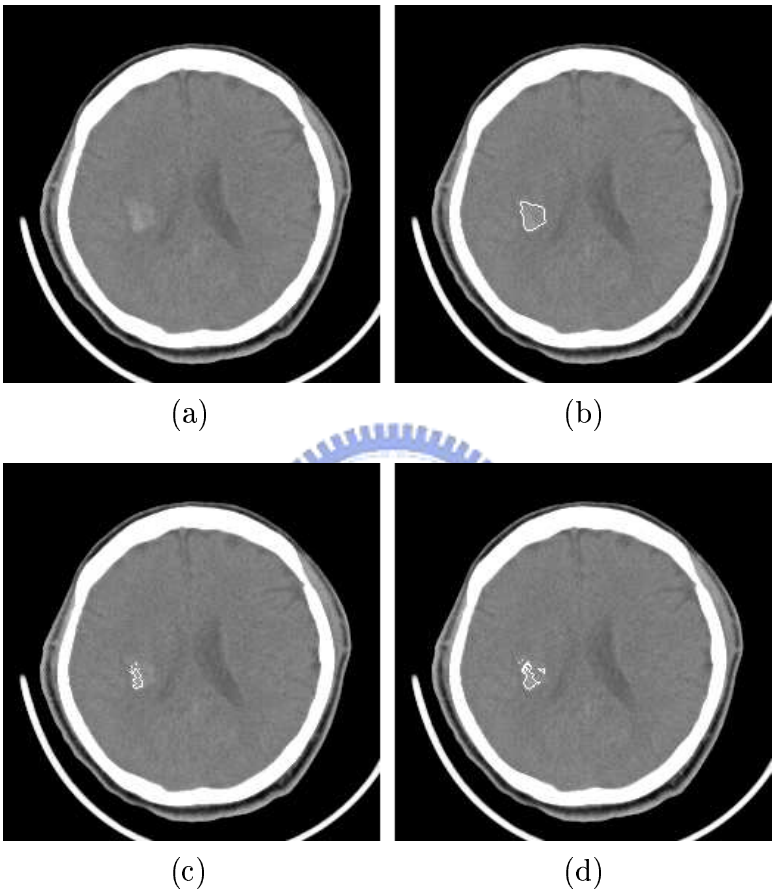

Figure 3.7: (a) The original CT image of human head. (b), (c), and (d) are the segmentation results using proposed approach, HKM, and FKM, respectively.

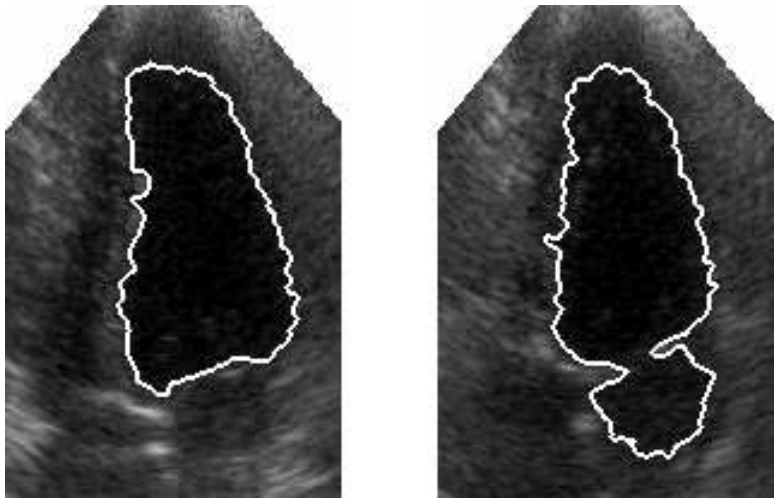

(a) (b)

Figure 3.8: (a) and (b) are two echocardiographic images with the boundaries obtained by the proposed approach.

$p(r_k) = n_k/n$, where r_k is the kth gray level, n_k is the number of pixels in the image with that gray level, and n is the total number of pixels in the image. We applied the hard c-means algorithm to divede the gray levels of histogram into clusters. These cluster centers are used for initial cluster centers of the proposed approach. Figure 3.10(a), (d) and (g) are the original images of CT, MR and echocardiography. Figure 3.10(b), (e) and (h) are the histograms with gray scales of Figure 3.10(a), (d) and (g), respectively. Figure 3.10(c), (f) and (i) are the segmentation results. When we applied the hard c-means algorithm to Figure 3.10(b), (e) and (h) for obtaining the initial cluster centers, the cluster number are 5, 4 and 4, respectively.

3.2.3 Discussions

The proposed approach requires initial values of gray scales for the cluster centers. The cluster centers could be obtained by understanding the images or analysis the histogram of the images with gray scales. In the most experiments, we gave the initial cluster centers with gray scales by our understanding of the images. We presented the good results in the experiments. In most of the cases of medical images segmentation, we know the average

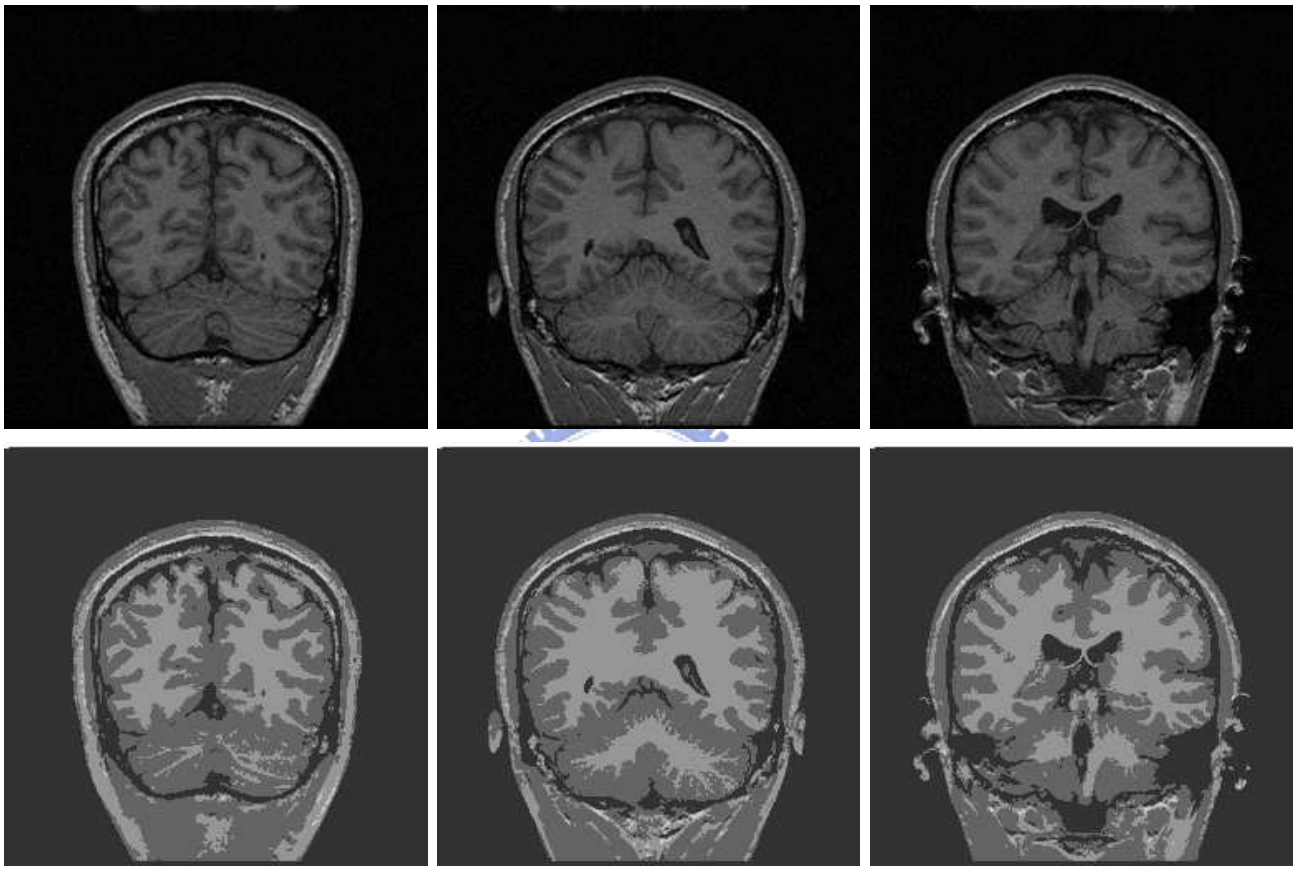

Figure 3.9: The pixels in the MR images are partitioned into 4 sets. From left to right, each column shows the original image (above) and the processed image (below).

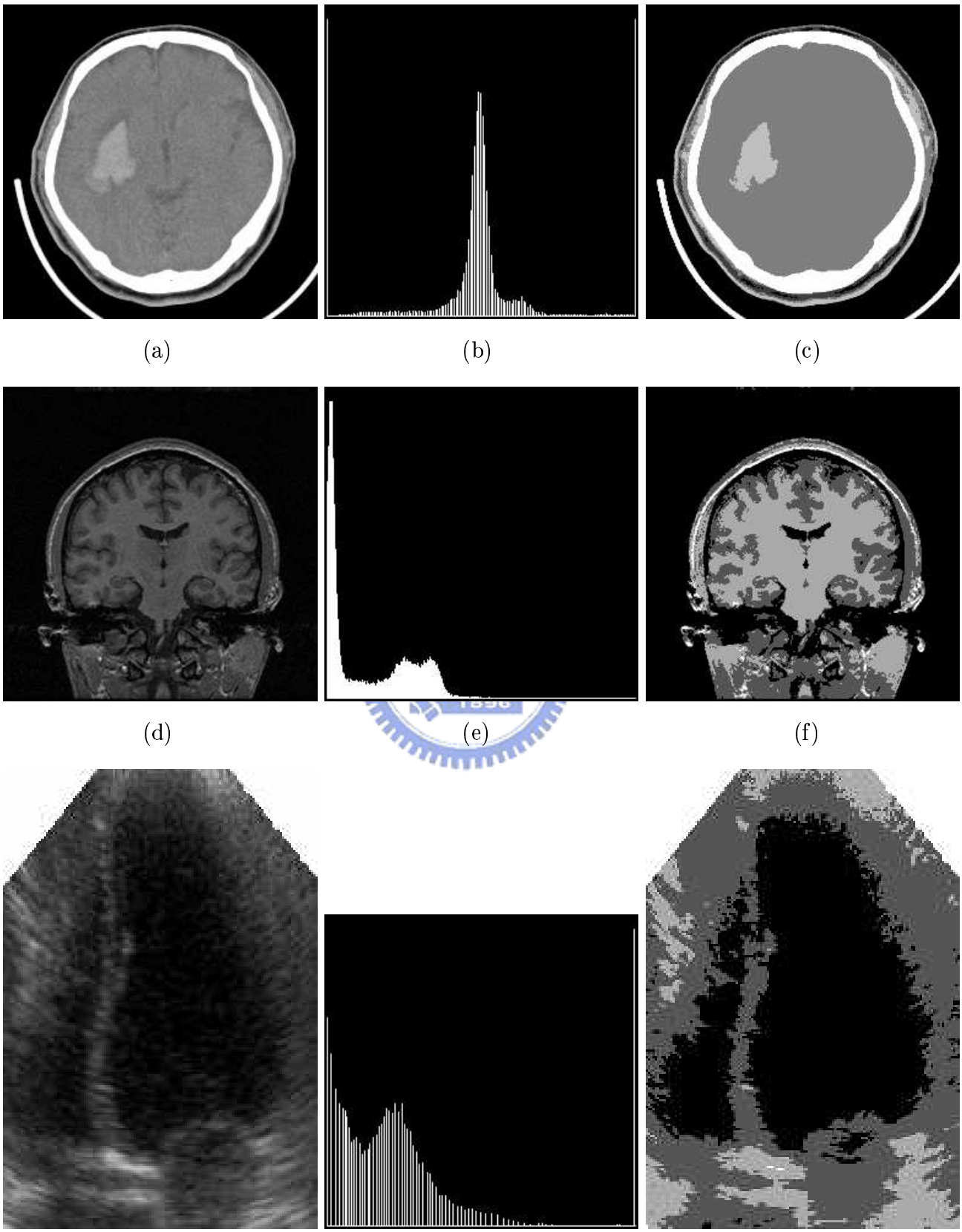

(a) (b) (c)

(d) (e) (f)

(g) (h) (i)

Figure 3.10: (a), (d) and (g) are the original images of CT, MR and echocardiography. (b), (e) and (h) are the histogram of (a), (d) and (g). (c), (f) and (i) are the segmentation results by first applying hard c-means algorithm for initial clustering then applying the proposed

intensity of the region of the interest. But it is not convenient for the clinical applications. We also provided an automatical technique to obtain the initial cluster centers in the last experiment. The cluster centers obtained by hard c-means algorithm with histogram which maybe not good enough espicially noisy image. If the segmented image is noisy or the region of interesting is very smaller than other regions, the number of cluster must be incremented. It is why the cluster number of Figure 3.10(a) and (g) are 5 and 4, respectively. Practically, the proposed approach can't accept the random initial cluster centers, but allows that the initial cluster centers aren't too far away from the actual cluster centers. It is difficulty to develop an automatical method for deciding very good initial cluster centers. Furthermore, comparing with the intensity thresholding method, the intensity threshold method is much more sensitive to the threshold value than the proposed method to the cluster centers.

3.3 Clustering Using α-shape Technique

Ultrasound instruments provide ultrasound images as well as the *Acoustic Quantitative* (**AQ**) images. AQ images display fluid and soft tissue in very different intensities. In general, fluid in an AQ image is displayed in a much lower intensities comparing to the soft tissue. Since the difference between the intensities of fluid and soft tissue is very significant, segmentation in AQ image is a much easier task. Lin reconstructed the LV endocardial surfaces from AQ images based on the physical based modeling[46]. However, the size of the heart chamber in an AQ image is generally smaller than the actual size. In order to get a more accurate volume, we still need to segment the heart chamber from the ultrasound images.

In this section, we present a clustering technique to segment the heart chamber from echocardiogram. The proposed algorithm, which is based on the α-shape of a set of points [22, 27], collects similar pixels into a set. The region of interest corresponds to one of the clusters under a properly selected α. Since there are generally hundreds images involved in calculating the volumes of heart chambers, it is not feasible to manually identifying the heart chambers

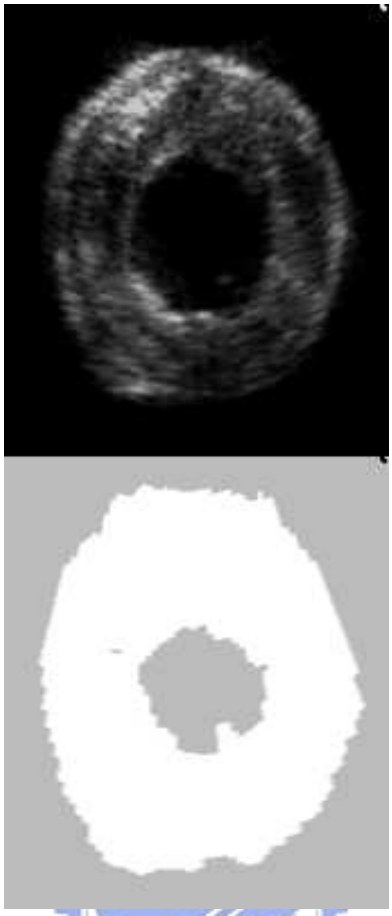

Figure 3.11: An example of echo image and its associated AQ image.

from all the images. We should develop an automatic method to segment the heart chambers.

The data set studied is a set of 4D echocardiogram acquired from a rabbit heart. A transthoracic transducer was used to acquired sequence of heart images using pull-back technique to obtain a set of 9 parallel cross sections. There are 24 sets of volume data to cover a systolic cycle. Volume of the heart chamber was controlled in the laboratory. The volumes of the heart chamber at the time the images acquired are known. The AQ images are also available. The upper image of Figure 3.11 is an example of the ultrasound images and the lower one is its associated AQ image.

3.3.1 α-shape and α-connectivity

In this subsection, we briefly describe the α-shape of a set of points in 3D space and its α-connectivity. We describe the α-shape without a formal definition. The details of the α-shape can be found in [27].

The α-shape mathematically defines the shape of a set of points in 3D space. An α-ball is a ball with radius α. The shape of a set of points is its convex hull when all the points can be enclosed by an α-ball. If an α-ball cannot enclose all the points, the shape is the union of all the convex hulls of all the subsets of the points which can be enclosed by an α-ball.

Given a set of n points, the shape of the point set is its convex hull when $\alpha = \infty$. As α decreasing, the shape becomes concave and then disconnected. If α is very small, the shape is n disconnected points. The α-shape might not be a 3D solid according to its definition. There are cases that some parts of the α-shape are line segments or triangles. The definition for the α-shape also defines the α-connectivity of points. Given a set of points S and an α, two points are α-connected if they are in the same cluster in its α-shape.

The α-shape and the α-connected components of a set of n points can be obtained from the Delaunay Triangulation of the point set. To compute the α connected components, we examine each Delaunay triangle whether it can be enclosed by an α-ball. If the Delaunay triangle can be enclosed in an α-ball, the four vertices of the Delaunay triangle are in the same connected component. For a given α, the α-connected components can be found efficiently using the Union-Find operation[38].

3.3.2 Proposed Method

In the proposed algorithm, we present an automatic method to extract the heart chamber from a set of 4D echocardiographic images. The need of an automatic method is due the huge number of images been processed. There are more than 200 images in a set of 4D volume data. It is not feasible to use an user interface approach to process the whole set of images

one by one. The proposed automatic method needs the AQ images. Extracting the heart chamber from an AQ image is a much easier job since an AQ image can be considered as a binary image. The heart chamber obtained from an AQ image is generally smaller than the actual heart chamber but it can be used as an reference for selecting α.

we identify the heart chamber in the ultrasound image by comparing the *similarity* between the α-connected components against the heart chamber obtained from the AQ image. Let A and B be two sets of pixels in an image and $C = A \cap B$. The number of pixels in A, B, and C are respectively $|A|$,$|B|$, and $|C|$. The similarity between A and B, denoted $SM_{(A,B)}$, is defined to be

$$SM_{(A,B)} = \frac{(|C|^2)}{(|A| \cdot |B|}).$$

The procedures to process each image are as the following.

1. Find the connected components of the low intensity pixels in the AQ image.

2. Determine the connected component that represents the heart chamber. Since the heart chamber is almost in the center of an image. The way to determine the heart chamber in the AQ image is to find a set of low intensity pixels that are the closest to the center of the image. The cluster having the largest number of pixels in the 25 by 25 square in the center of an image is the cluster representing the heart chamber. Let the set of pixels be denoted H.

3. Calculate all the α-connected components that are sufficiently large. We calculate the 30 largest connected components for each α.

4. Compute the similarity between all the α-connected components obtained in the previous step against H. The cluster that the most similar to H is the heart chamber in the ultrasound image.

3.3.3 Experimental Results

The proposed approach has been tested by a data set of echocardiographic images in our experiments. Figure 3.12 shows a set of experimental results of the extracted boundaries of heart chambers by proposed algorithm. The boundaries of AQ images are drawn in original images which are shown in Figure 3.13. In Figure 3.14, we also drawn both boundaries of the heart chamber of the proposed algorithm and AQ for easily comparison. The heart chambers obtained by our approach is closer to the actual heart chambers than the heart chambers obtained from AQ images.

We then applied the automatic method to process the 4D volume data set. The automatic method extracted the heart chambers from all the images without an user interface. We then compute the volumes of the heart chambers at each time in a systolic cycle. Since we know the true volumes, we compare the computed results against the true volumes. The final result is shown in Figure 3.15. Our result is more accurate than that obtained from the AQ images.

To calculate the ejection rate is one of the most important tasks. The actual ejection rate is 2.184. The ejection rates obtained from the proposed automatic method and the AQ image are respectively 2.38 and 2.76.

3.3.4 Discussions

We applied the automatic method to process the whole set of the 4D volume data. The automatic method extracted the heart chambers from all the images without an user interface. We compared the computed results against the true volumes. The final result is shown in Figure 3.12. The proposed method can get better results than that obtained from the AQ images.

To calculate the ejection rate is one of the most important tasks. The actual ejection rate is 2.184. The ejection rates obtained from the proposed automatic method and the AQ image are respectively 2.38 and 2.76.

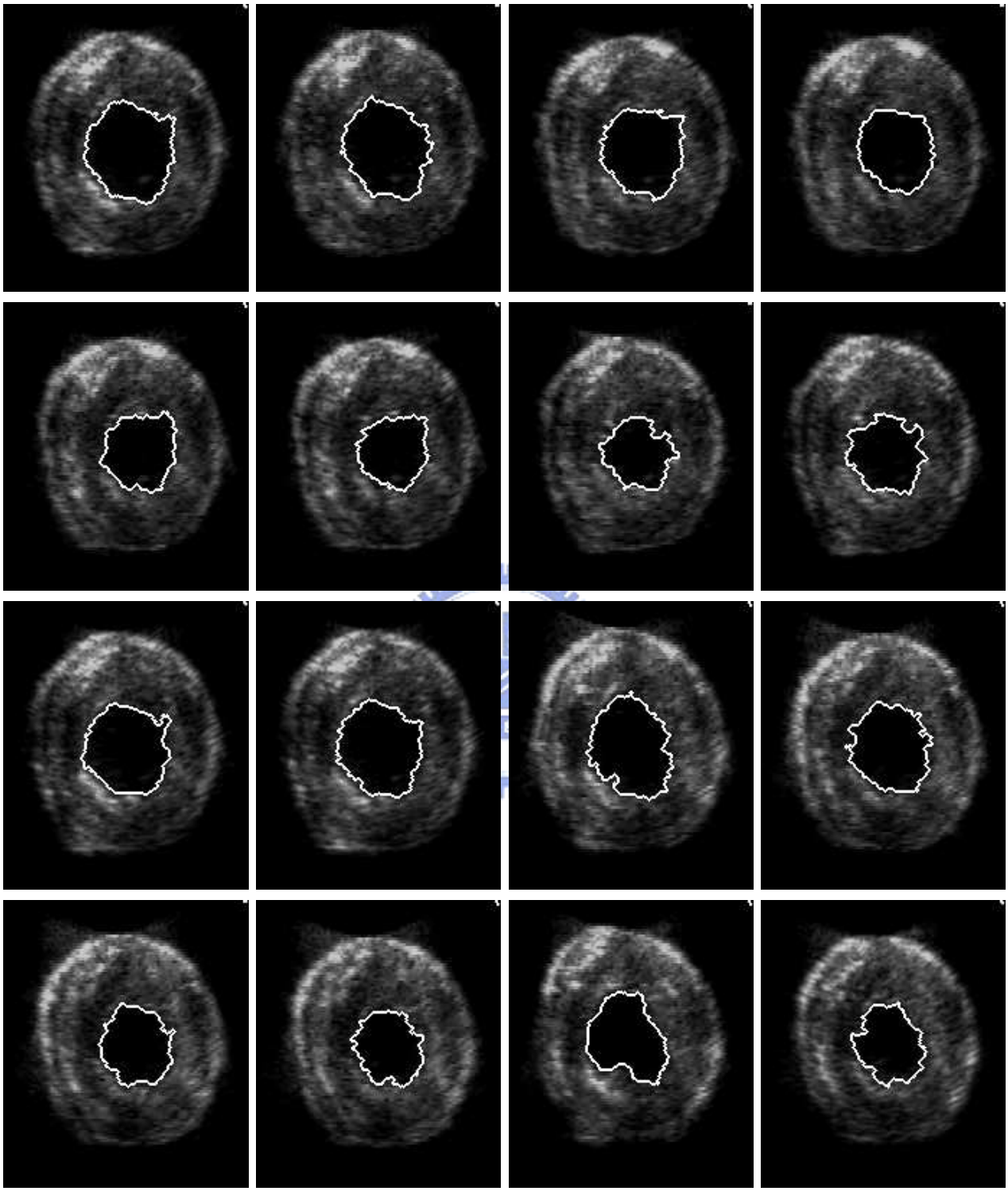

Figure 3.12: A set of experimental results of the extracted boundaries of heart chambers by proposed algorithm.

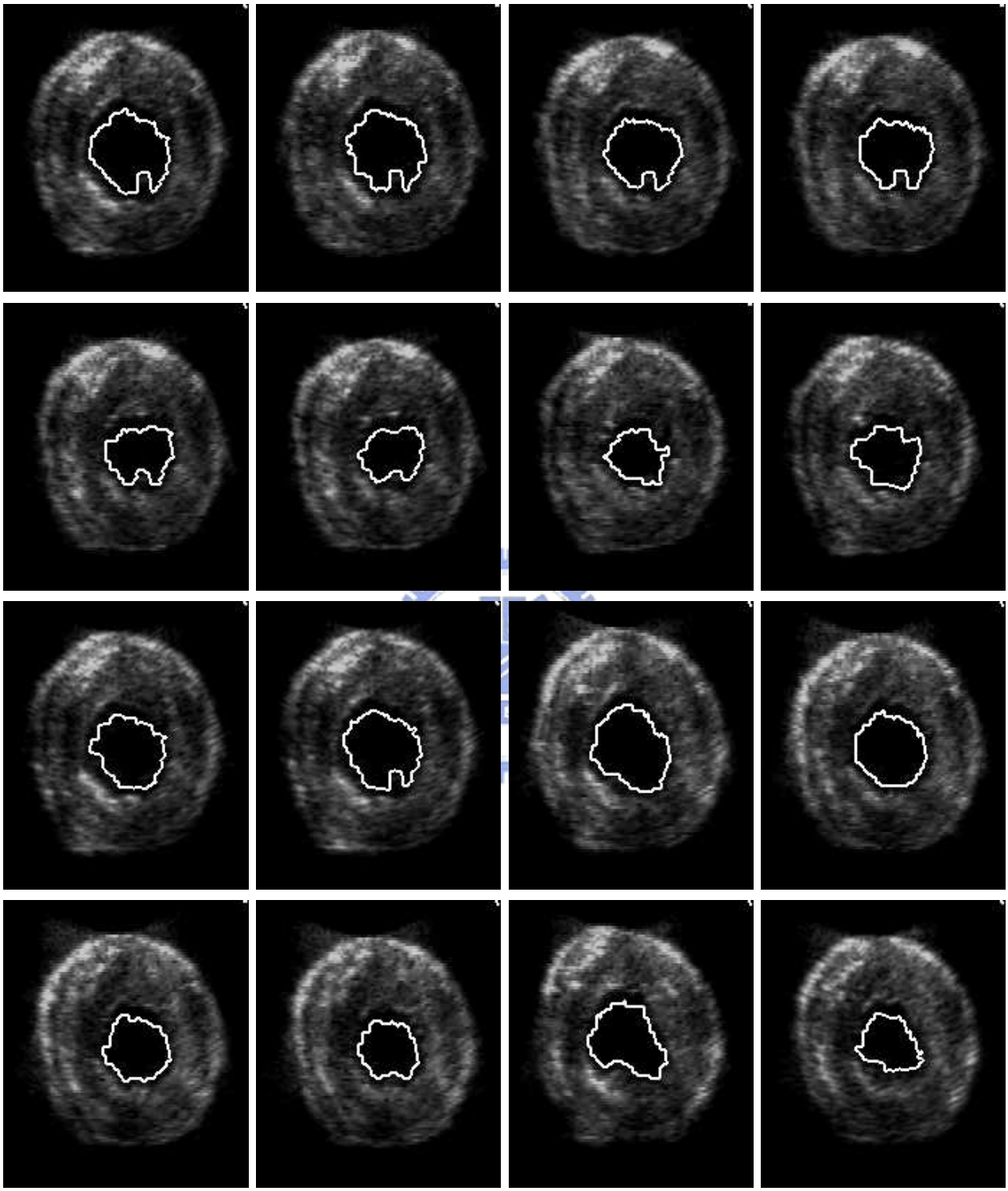

Figure 3.13: A set of boundaries of AQ images drawn in original images.

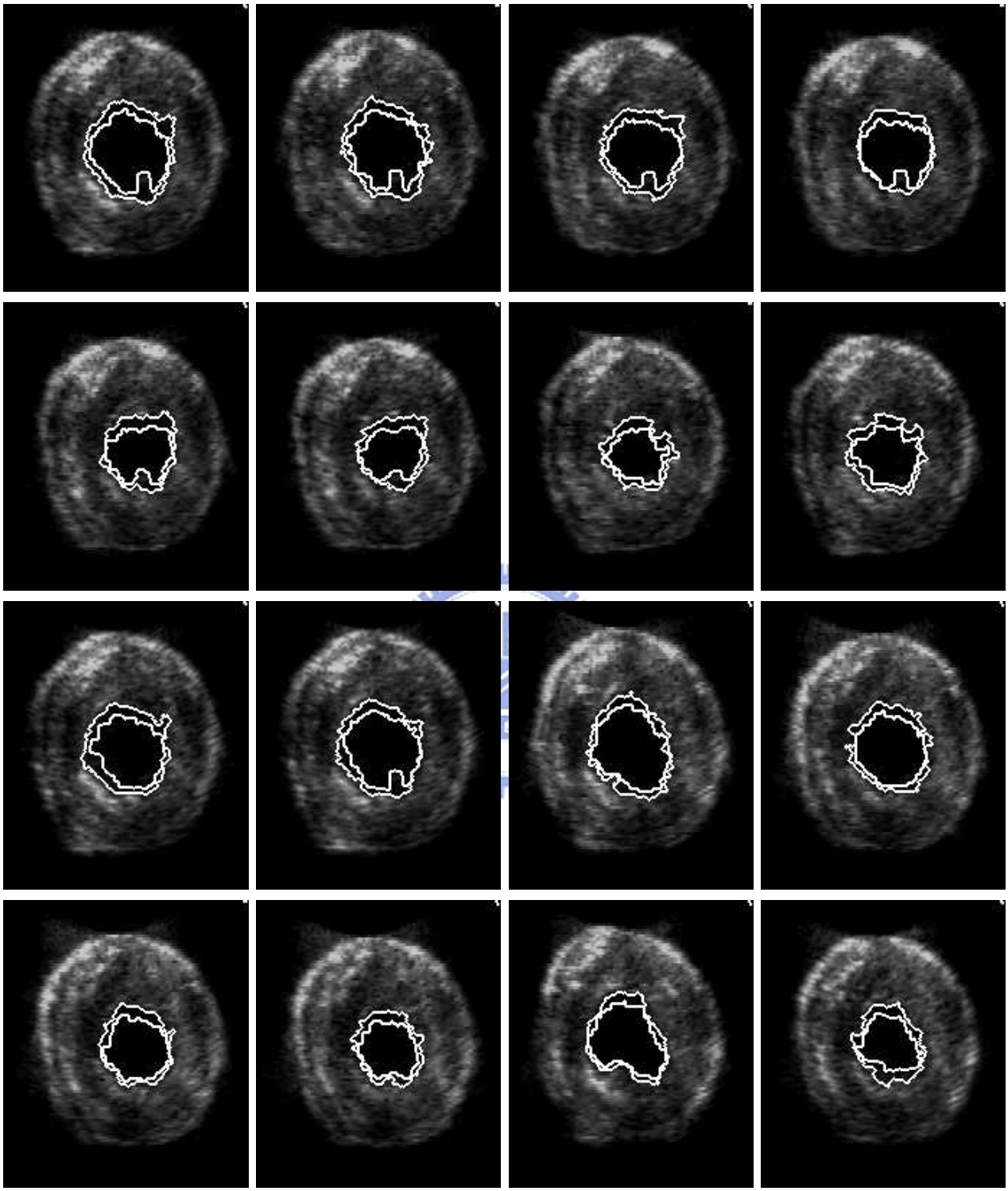

Figure 3.14: A set of both boundaries of the heart chamber of the proposed algorithm and AQ for easily comparison.

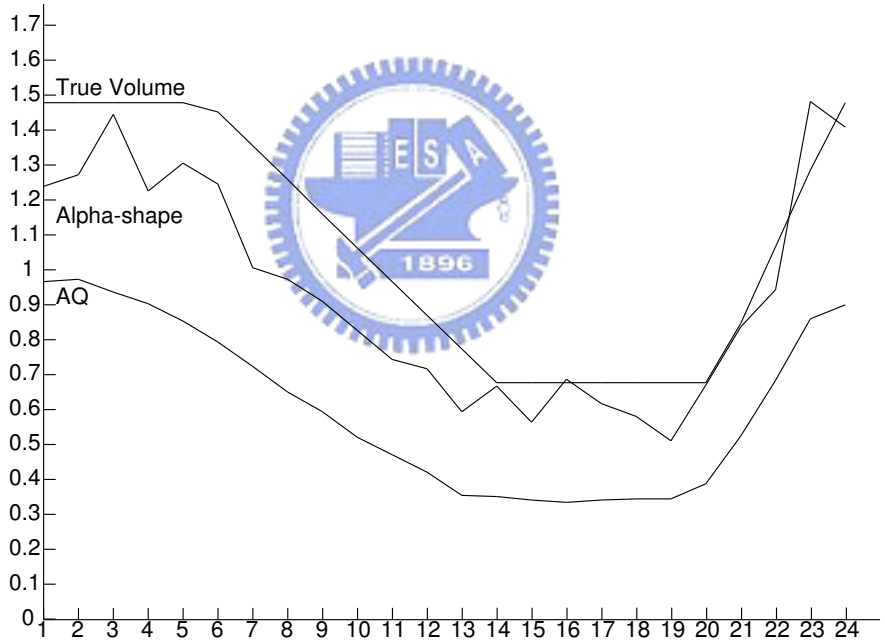

Figure 3.15: There are 24 image frames to cover a systolic cycle. The x-axis is the image frames and y-axis is the volume. The three curves are respectively the curves for the True Volumes, the volumes obtained by α-shape approach and the volumes obtained from AQ images.

The proposed segmentation algorithm worked well when the region of interests were sufficiently large. In our experiments, there were more than one thousand α-connected components for an α. Most of them contained only a very small number of points. If the region of interest is small, it is hard to identify the region of interest among the small clusters.

As shown in Figure 3.15, the heart chambers calculated by our algorithm tends to be smaller than the true volumes. This is because we used the heart chambers in AQ images as references to determine the α-connected components. To find the connected component of the heart chamber without help of AQ images is proposed as a future work.

3.4 Summary

In this study, we have proposed two region-based algorithms for echocardiographic image segmentation. The first one is the fuzzy Hopfield neural network with fixed weight method. In the proposed approach, we incorporate the global gray-level information to perform the initial clustering, then used the local gray-level information to construct the fuzzy Hopfiled neural network. We used a fuzzy set to represent the output states. A fixed weights approach was applied to improve the performance. According to our experiments, the performance of the proposed approach is much better than the hard c-means, fuzzy c-means and CHNN methods. We applied the proposed method to real medical images. The proposed method can worked well overcome the half volume problem in CT images and noise in cardiac ultrasound images.

The other proposed algorithm is the clustering method using α-shape technique. The proposed algorithm is based on the α-shape of a set of points to collect the similar pixels into a set. When we select a proper α, the region of interest is corresponding to one of the clusters. The heart chamber is determined by comparing the similarity between the α-connected components against the heart chamber obtained from the AQ image. The proposed algorithm is tested by a data set of ultrasonic images of rabbit heart. Experimental results show that the proposed algorithm could find a more accurate heart chamber than the heart

chamber obtained from AQ images. We also noticed that we could always find an α so that there is a cluster which could well approximate the heart chamber. But it is hard to determine the best α and the cluster if AQ images are not available.

Chapter 4

Edge Based Approach Using Shortest Path Algorithm

4.1 Introduction

Edge-based segmentation approaches use the postulate that the pixel values change rapidly at the boundary between two regions. The basic method is to apply a gradient operator such as the Sobel or Prewitt filter. High values of this filter provide candidates for region boundaries, which must then be modified to produce closed curves representing the boundaries between regions. Converting the edge pixel candidates to boundaries of the regions of insterest is a difficult task.

Due to the presence of noise of the original image, during edge detection it is possible to locate intensity changes where edges do not exist. For similar reasons, it is also possible to completely miss existing edges. Edge localization is another problem encountered in edge detection. The addition of noise to an image can cause the position of the detected edge to be shifted from its true location. The ability of an edge-detector to locate in noisy data an edge that is as close as possible to its true position in the image is an important factor in determining its performance.

In this study, we propose two edge-based segmentation approaches for extracting heart chamber. If the heart chamber is star-shaped, such as the rabbit heart, we ciraularly spread the image and then construct a directed graph to find the shortest path for extracting the

boundary of heart chamber. The definition of star-shaped can be found in [62]. An object O is star-shaped if there exists a point z not external to O such that for all points o of O the line segmentation $\overline{zo}$ lies entirely within O. Thus, each convex is also star-shaped. The locus of the points z having the above property is the *kernel* of O. Thus, a convex coincides with its own kernel. There is a hierarchy that is strictly ordered by the subset relation

$$\textbf{Convex} \subset \textbf{Star-Shape} \subset \textbf{General}.$$

We also extended the shortest path finding algorithm to a general case, such as the left ventricle of human heart.

The remainder of this chapter is organized as follows. In Section 4.2, we present the proposed algorithm using a directed graph for detecting boundary of heart chamber which is star-shaped. We extend this approach to a general case in Chapter 4.3. In the last section, concluding remark is include.

4.2 Heart Chamber is Star-Shaped

In this section, we focus on the star-shaped heart chamber, such as a rabbit heart. It is supposed that the image center locates the kernel of the star-shaped heart chamber. Due to the property of star-shaped described in the definition of above introduction, the original image is transfer to a circularly spread image. We use both first and second derivative edge detectors for edge detection and then map the image into a directed graph. In the directed graph, we find the shortest path by dynamic programming algorithm. The cardiac boundary is obtained by backmapping the shortest path into the original image.

4.2.1 Proposed Method

In the proposed algorithm, we present a new approach to extract the cardiac border. The shortest path of directed graph is applied in the proposed approach. The result border should be a smooth curve and go through the high gradient points. Depending on this rule, we give

(a) (b)

Figure 4.1: (a) original cardiac image (b) spread image from (a).

the weight of edges and vertices on the directed graph.

In the first step, we spread the echocardiographic image in the circular direction. The location on a radial line from the center is assigned as the vertical axis and the angle of the line is assigned as the horizontal axis in the spread image, as shown Figure 1. From bottom to up, the spread image has three layers: fluid, soft tissue, and background. The spread image is produced from original image. The coordinate transformation of circularly spread can be presented as follow:

$$T(x, y) = O(y \cdot \cos(x), y \cdot \sin(x)), 1 \leq x \leq m, 1 \leq y \leq n, \tag{4.1}$$

where $T(x, y)$ and $O(x, y)$ is the intensity of coordinate (x, y) in spread and original images, respectively, and m and n are the image size of column and row of spread image, respectively. If $O(x, y)$ doesn't locate at grid point, bi-linear interpolation will be used to determine it.

In the spread image, the cardiac boundary on the spread image is a horizontal line from left to right. The border line can be traced from the leftest column to the rightest column.

In the second step, we construct a weighted, directed graph for edge detection applications. A graph consists of a set of vertices and a set of edges that determine how the vertices can be connected. In edge detection applications, the vertices generally correspond to pixels of the image and the edges determine the connection of pixels to form borders. So the size of vertex in the graph equals to the size of spread image. In the other word, if the spread image is a $n \times m$ image, the size of vertex in the graph is m columns and n rows. Each vertex in column

i is linked to each vertex in the succeeding column, column $i+1$, on the graph. Each path from column 1 to column m is a possible solution to the edge detection problem. The optimal or shortest path represents the best border in the case of edge detection.

There are weights associated with all the vertices and all the edges. The weights are designed so that the shortest directed path from v_{0_j} to v_{m_j}, for all j, corresponds to endocardial wall in the image.

The weights on the vertex v_{i_j} and edge $e_{i_{(j,k)}}$, denoted $w(v_{i_j})$ and $w(e_{i_{(j,k)}})$ are determined as the following equations,

$$w(v_{i_j}) = (-MH(v_{i_j}) - Sobel(v_{i_j})) \cdot \sin(GD(v_{i_j}), \tag{4.2}$$

$$w(e_{i_{j,k}}) = (j-k)^2, \tag{4.3}$$

where $MH(v_{ij})$ and $Sobel(v_{ij})$ are the magnitude of Marr-Hildreth and Sobel filters on v_{i_j}, respectively, and $GD(v_{ij})$ is the gradient direction on v_{i_j}.

Marr and Hildreth's theory [51] is filtered an image by a Laplacian-of-Gaussian (LoG) kernel

$$LoG(r) = \bigtriangledown^2 G(r) = \frac{-1}{2\pi\sigma^4}\left[2 - \frac{r^2}{\sigma^2}\right] exp\left(-\frac{r^2}{2\sigma^2}\right) \tag{4.4}$$

where $r = \sqrt{x^2+y^2}$ is the distance from the mask center, $G(r) = \frac{1}{2\pi\sigma^2} exp\left(-\frac{r^2}{2\sigma^2}\right)$ is an isotropic 2-D Gaussian, and σ is its standard deviation. The Laplacian $\bigtriangledown^2$ is a second-order differential operator, edge points are individuated by the zero-crossing of the filtered image. The combination of $\bigtriangledown^2$ with a Gaussian mask permits the smoothing out the noise, which is controlled by the σ pamameter; the larger σ, the stronger the blurring. The weight of a vertex is inversely related to the likelihood that an edge is presented at that point. The likelihood value is then converted to a weight that the greater the edge strength, the lower the weight of the vertex. The Sobel's and Marr-Hildreth's filters are used for edge points detection. The term of gradient direction is the consideration of a priori knowledgement that classify which border we want. In the case of cardiac border extraction, Figure 4.1 shows two borders in

the spread image. The different border has different gradient direction. The correct gradient direction is needed to improve performance. In the echocardiographic image, the intensity of fluid region is lower than soft tissue. The gradient direction of endocardial border is 90 degree, so $\cos(GD)$ can be used for endocardial border classification.

The third step is finding the shortest path from column 1 to column m. The path $p(v_1, v_2, ..., v_m)$ from v_1 to v_m is a sequence of vertices which go through $v_1, v_2, ..., v_m$, where v_i is one of the vertices in column i. We use a dynamic programming algorithm to find the shortest path. The desired border is a closed contour. So we determine the weight of a path $p(v_1, v_2, ..., v_m)$ as

$$w(p(v_1, v_2, ..., v_m)) = w(v_1) + w(e(v_1, v_2)) + w(v_2) + ... + w(v_m) + w(v(v_m, v_1)). \quad (4.5)$$

The shortest path from v_{11}, v_{12},..., and v_{1n} are found, respectively. The shortest path algorithm from v_{11} by dynamic programming is as follow:

1) For every v_3, tabulate the v_2 that determines the shortest path from v_{11} to every v_3:

$$S(v_{11}, v_{3j}) = \min\{w(v_{11}) + w(e_{11i}) + w(v_{2i}) + w(e_{2ij}) + w(v_{3j})\}, 1 \leq i, j \leq n, \quad (4.6)$$

$$(4.7)$$

2) For every v_4, tabulate the v_3 that determines the shortest path from v_{11} to every v_4:

$$S(v_{11}, v_{4j}) = \min\{S(v_{11}, v_{3i}) + w(e_{3ij}) + w(v_{4j})\}, 1 \leq i, j \leq n, \quad (4.8)$$

$$(4.9)$$

3) Repeat the similar procedures to last column. For every v_m, tabulate the v_{m-1} that determines the shortest path from v_{11} to every v_m:

$$S(v_{11}, v_{mj}) = \min\{S(v_{11}, v_{(m-1)i}) + w(e_{(m-1)ij}) + w(v_{mj}) + w(e(v_{mj}, v_{11})), 1 \leq i, j \leq n. \quad (4.10)$$

4) Find the shortest path form v_{11} is the minimal weight of $S(v_{11}, v_{mi}), 1 \leq i \leq n$.

The same algorithm are also used to find the shortest path from v_{12}, v_{13},..., v_{1n}. The minimal weight of these n shortest path is the desired border.

The final step is backmapping the shortest path to original image for cardiac boundary extraction. The transformation of cardiac border from spread image to original image is presented by follow:

$$O_k(x) = T_k(y) \cdot \cos(T_k(x)), \tag{4.11}$$

$$O_k(y) = T_k(y) \cdot \sin(T_k(x)), \tag{4.12}$$

where $O_k(x)$ and $O_k(y)$ are the x and y coordinate of k-th vertex in original image, and $T_k(x)$ and $T_k(y)$ are the x and y coordinate of k-th vertex in spread images.

4.2.2 Experimental Results

The proposed method has been tested by using a data set acquired from a rabbit heart. The volume of the heart chamber at the time that the images were acquired is known. A transthoracic transducer was used to acquired sequence of heart images with pull-back technique to obtain a set of 9 parallel cross sections. There are 24 sets of data to cover a cardiac cycle.

In this experiment, the size of original images is 200×170. We transfer the original image into a spread image which size is 360×170. The weighted, directed graph is constructed with 61200 vertices and 10115000 edges. The spread image was smoothed by a Gaussian filter (standard deviation $\sigma = 1.8$). The optimal parameter value σ was selected after several trials. Figure 4.2 (a) is one of the original images. The circularly spread image of Figure 4.2 (a) is shown in Figure 4.2 (b). Figure 4.3 shows four of the results of the cardiac boundary extraction on the data set by proposed algorithm. The results demonstrate that we provide pretty good approximation for the cardiac boundary by proposed approach.

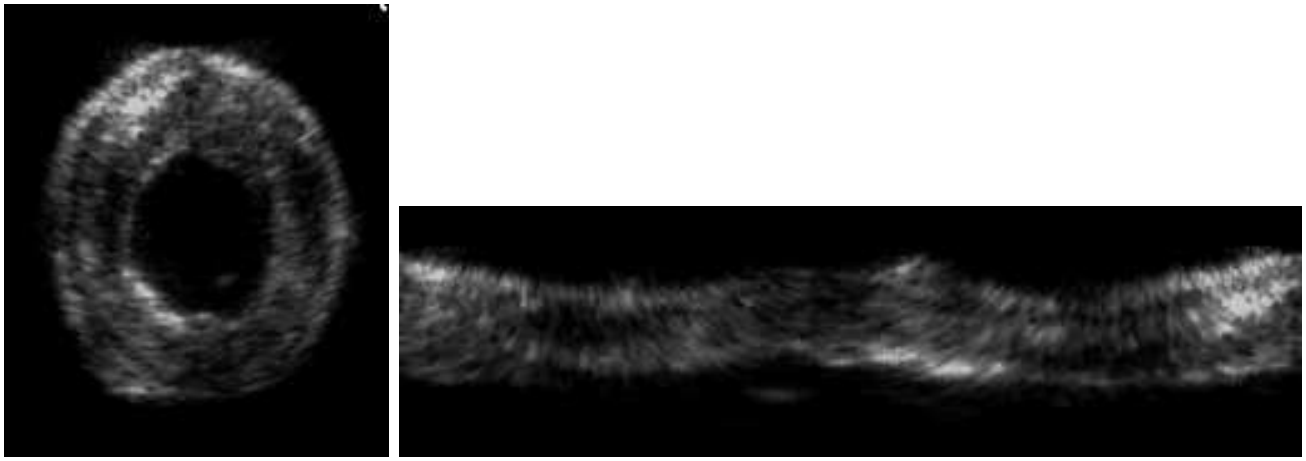

(a) (b)

Figure 4.2: Original image (a) and the spread image (b).

4.2.3 Discussions

In this chapter, we proposed a new approach for cardiac boundary extraction on echocardiographic images by directed graph. In this approach, we spread the cardiac image in the circular direction. The spread image is mapping to a directed graph. The shortest path is found by the dynamic programming algorithm. From the implemented results, we can obtain pretty good approximation for cardiac boundary extraction.

The echocardiographic images are normally noisy. It is difficult that a point with big magnitude of gradient is not selected for constructing a boundary, but a point with small magnitude of gradient is. Because that the shortest path has the minimal weight between all the possible paths, it may not go through the largest highest frequence point. For the same reason, the shortest path may go through the points that their gradient magnitude is small. Due to the shortset path is searched exactly one point in each column, the extracted cardiac boundary is ensured that it is closed. Experimental results demonstrated that the contour of the circular like object is easily detected by using the spread image and the boundary extraction algorithm. The proposed algorithm is only proper for the circular like objects. The problem of the complex contour extraction is resolvable in the next chapter.

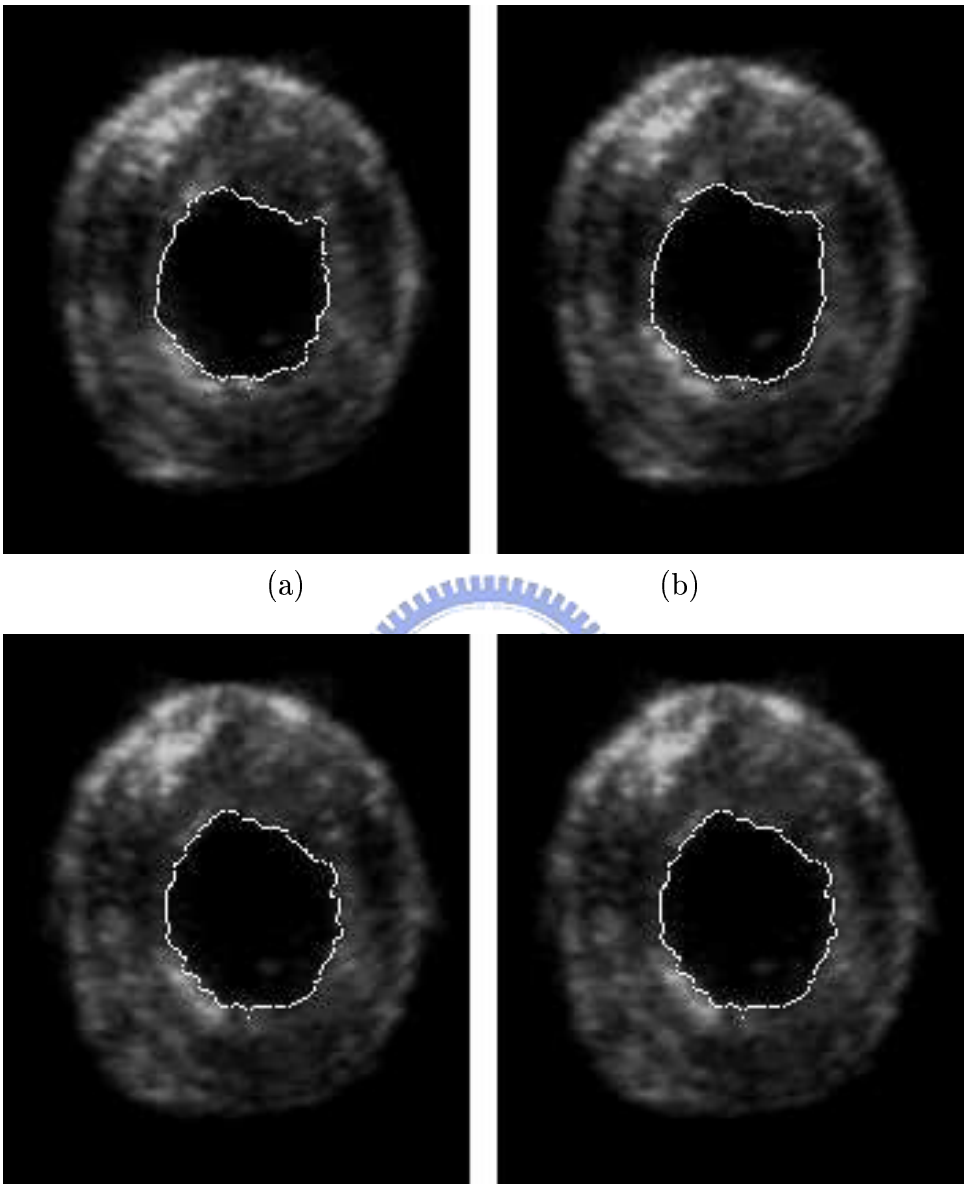

Figure 4.3: The results of cardiac border extraction

4.3 General Case

According to searching the shortest path of the directed graph described for extracting the star-shaped heart chamber in the last section, we propose an adaptive approach for boundary extraction in a general case, such as the boundary of left ventricle, also based on searching the shortest path algorithm. We first detect the edge points for the given images using the Sobel operator, and then construct the search space from the edge images using α-contour technique. The directed graph is mapped from the constructed search space and the shortest path is searched as we mentioned in the last section.

The remainder of this chapter is organized as follows. An adaptive approach for extracting the left ventricle is described in Section 4.3.1. In Section 4.3.2 we present the results obtained by the proposed algorithn. Discussions are given in Section 4.3.3

4.3.1 Proposed Method

The echocardiographic image is processed by high-pass filter to enhance the high-frequency points and then threshold the filtered image by a threshold value to obtain the edge image. The edge image is applied the alpha-contour approach to obtain the contour image. The points of inner and outer contours are triangulated to construct the search space. The search space is constructed by a weighted directed graph which using the edges of triangles. The active contour model, so called snake model, is applied to an energy function for contour extraction. We use the dynamic programming approach for finding the shortest path in the directed graph. The final step is back-mapping the shortest path to original image for cardiac contour extraction.

Initial contour selection with High-pass Filtering and α-contour

The first stage in deformable contour model is the initial contour selection. It is selected by manual input or interactive template matching in the conventional approaches. We will

develop a near automatic procedure for initial contour selection. The first step is filtered the echocardiographic images by high-pass filter. We incorporate the Sobel operator introduced in Section 2.4 for high-pass filter to produce the candidates for initial contour.

The next step is separating the candidates of high-frequency points into some clusters by α-connected component. The α-shape and the α-connectivity of a set of points in 3D space is briefly decribed in Section 3.3.1. The α-contour is defined as the boundary of the α-connected component. We select the maximal cluster of α-contour as initial contour for deformable contour model.

Dilation

Dilation is one of the bases for most of the morphological operations. The other morphological operations are presented in [35]. The language of mathematical morphology is set theory. Sets in mathematical morphology represent the shapes of objects in an image. For example, the set of all the black pixels in a binary image is a complete description of the binary image. In binary images, the sets in Euclidean 2-space denote foreground regions. Many of the operations can be formulated in terms of n-dimensional Euclidean space, E^n. However, we focus on binary images whose components are elements of Z^2. The details of higher dimensional spaces of mathematical morphology are introduced in [30].

Let A and B be sets in Z^2, with components $a = (a_1, a_2)$ and $b = (b_1, b_2)$, respectively. The *translation* of A by $x = (x_1, x_2)$, denoted $(A)_x$ is defined as

$$(A)_x = \{c | c = a + x, \text{ for } a \in A\}. \tag{4.13}$$

The *reflection* of B, denoted $\hat{B}$, is defined as

$$\hat{B} = \{x | x = -b, \text{ for } b \in B\}. \tag{4.14}$$

With A and B as sets in Z^2 and $\emptyset$ denoting the empty set, the *dilation* of A by B, denoted $A \oplus B$, is defined as

$$A \oplus B = \{x | (\hat{B})_x \subset A \neq \emptyset\}. \tag{4.15}$$

Thus the dilation process consists of obtaining the reflection of B about its origin and then shifting this reflection by x. The dilation of A by B then is the set of all x displacements such that $\hat{B}$ and A overlap by at least one nonzero element. Set B is commonly referred to as the structuring element in dilation, as well as in other morphological operations.

Search the Shortest Path from Constructed Directed Graph

The weighted directed graph, $G(V, E)$, is constructed by using the edges which cross the inner and outer contours. The vertex V is the union of the vertex sets V_i, $i = 0, \ldots, m$, where each vertex in V_i corresponds to a pixel in the ith column. V_m corresponds to the firts column. Each vertex in V_i has n directed edge connecting to all of the vertices in V_{i+1}. The jth vertex in V_i is denoted v_{i_j}. Since the vertex v_{i_j} can only connect to a vertex in V_{i+1}, the directed edge connecting v_{i_j} and the kth vertex in V_{i+1} is denoted $e_{i_{(j,k)}}$. The number of vertices and the number of edges are respectively $m \cdot n$ and $m \cdot n^2$. Each path from column 1 to column m is a possible solution to the edge detection problem. The optimal or shortest path represents the best border in the case of edge detection. The weights of vertices and edges are determined and the shortest path is searched in the directed graph by the same method presented in the last section. The shortest path is backmapped into the original image for cardiac boundary extraction.

Summary of the proposed algorithm

The proposed segmentation algorithm is summarized as follows:

Step 1) The original image is processed by Sobel filter for high-pass filtering. The high frequence points are the candidates of the boundary.

Step 2) The candidates are clustered into some α-contours. The maximal one of the α-contours is the initial contour.

Step 3) The initial contour is increased the thickness by dilation operation. The boundary of the thicked contour construct the inner and outer contours.

Step 4) The points located on the inner and outer contour are triangulated. The edges across the inner and outer contour are used to constrct a directed graph.

Step 5) The shortest path is calculated by searching technique proposed in Section 4.2.

The final step is backmapping the shortest path into the original image for cardiac boundary extraction.

4.3.2 Experimental Results

The proposed method has been tested by a data set of echocardiographic images. Figure 4.4 (a) is one of the original echocardiographic images. We processed the original image by Sobel operator to enhance the high-frequency points and then threshold it to obtain the edge image. As shown in Figure 4.4 (b), the filtered points are difficult to classify them for extracting the boundary of left ventricle. The α-contours are determined by the boundaries of α-connected components of the edge points as shown in Figure 4.4 (c). There are a number of connected components in the α-contours. The maximal one is the initial contour for left ventricle extraction in the following steps.

The initial contour is increased the thickness by *dilation* operation, as shown in Figure 4.5 (a). The boundary of the thicked contour construct the inner and outer contours for search space. Figure 4.5 (c) is the triangulation of the points located on inner and outer contours. We chech each edge of all triangles. If the two end-points of the edges across the inner and outer contours, they are remained to construct the search space within a directed graph, as shown in Figure 4.5 (d). We Calculated the shortest path in the directed graph, and then back-mapping the shortest path to original image for left ventricle extraction. Figure 4.6 shows the extracting result of left ventricle on echocardiographic image. We also showed another two results of left ventricle extraction in Figure 4.7.

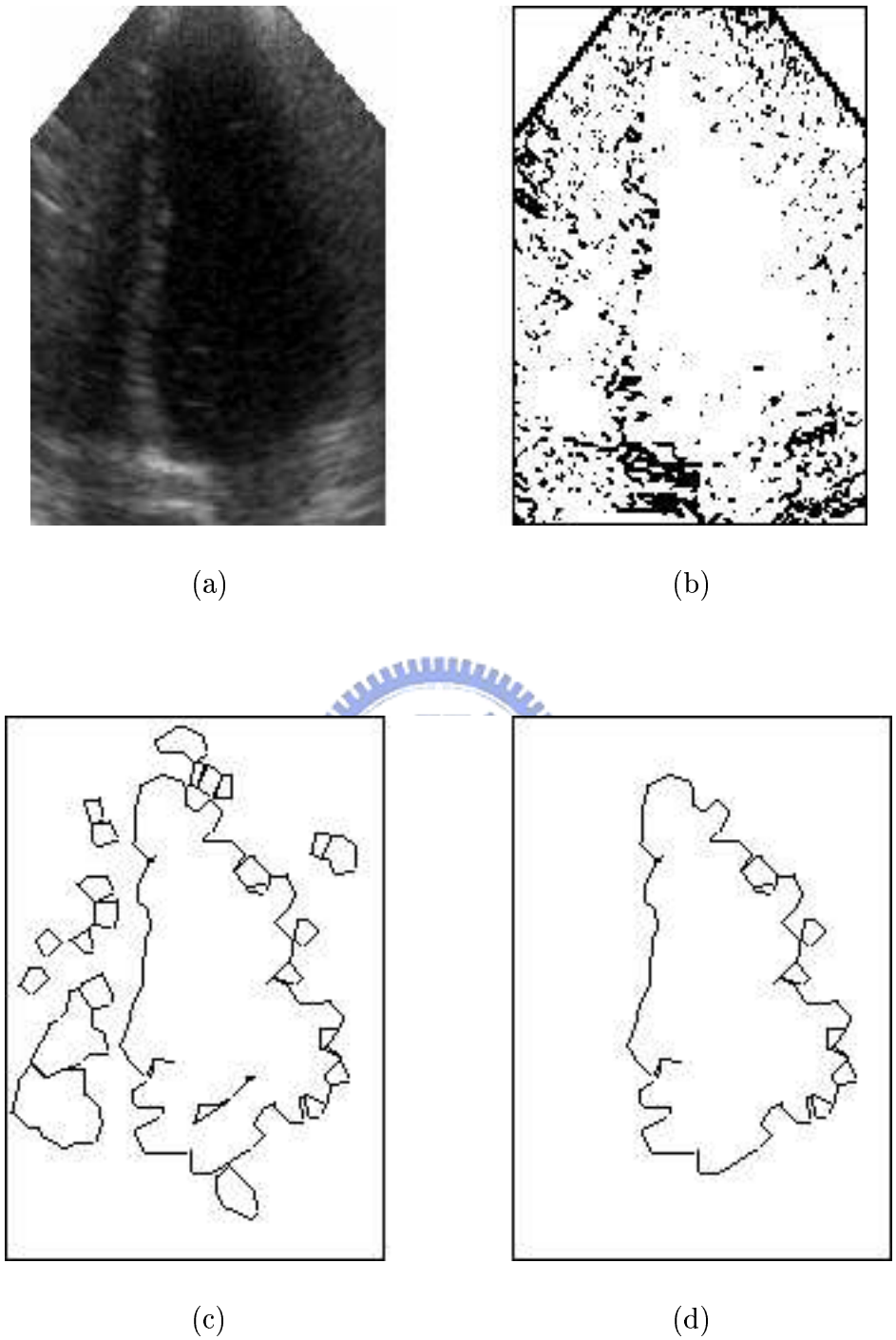

Figure 4.4: (a) One of the original echocardiographic image; (b) Highpass filtered image of (a) by Sobel operator; (c) α-contour of the points in (b); (d) The maximal connected component in (c).

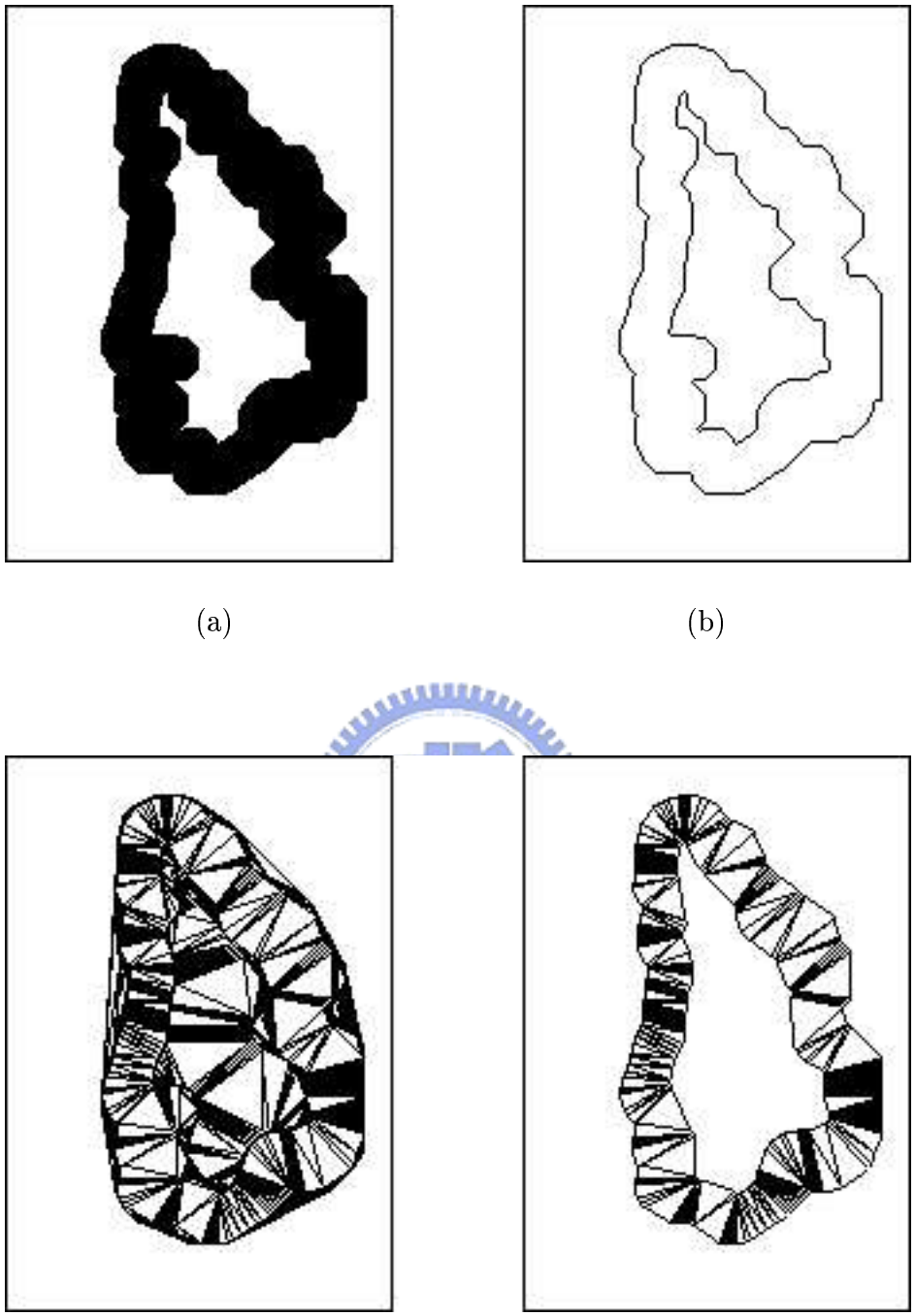

Figure 4.5: (a) The thick contour of initial contour processed by dilation operation; (b) The inner and outer contours of search space; (c) The triangulation of the points located on the inner and outer contours; (d) The edges which across inner and outer contours on (c).

Figure 4.6: The extraction result of left ventricle on the echocardiographic image.

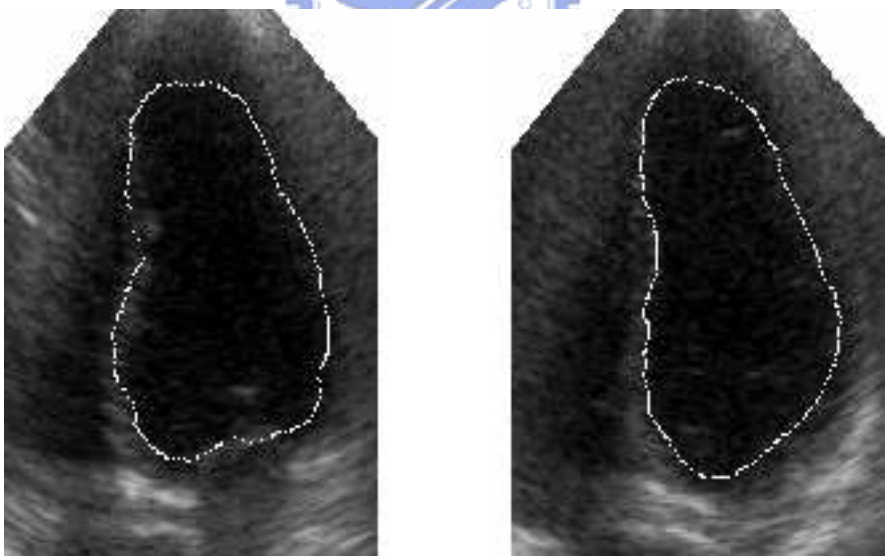

(a) (b)

Figure 4.7: The other extraction result of left ventricle.

4.3.3 Discussions

In this section, we proposed a new approach for cardiac boundary extraction on echocardiographic images. An α-contour approach based on α-shape technique is proposed to process the edge image for grouping the edge points into contours. The triangulation of the vertices located on inner and outer contours construct the search space for performing the snake model. To avoid the local minimum trapping, dynamic programming approach is used for finding the shortest path. From the implemented results, we can obtain pretty good approximation for cardiac boundary extraction.

The proposed method has been tested by a data set of echocardiographic images. When we extract the cardiac boundary of whole set of cardiac graphic images, we can calculate the cardiac volumes in whole cardiac cycle. If we compare the cardiac volume in the end-diastolic and end-systolic images, the ejection rate can be calculated.

4.4 Summary

In this study, we have proposed two edge-based algorithms for echocardiographic image segmentation. These two approaches both find the shortest path in a directed graph for boundary extraction of the heart chamber. If the heart chamber is star-shaped, such as the rabbit heart, we propose the shortest path finding algorithm to extract the boundary of heart chamber. In this approach, we spread the cardiac image in the circular direction. The spread image is mapping to a directed graph. The shortest path is found by the dynamic programming algorithm.

We extend the shortest path finding algorithm to a general case. An alpha-contour approach based on alpha-shape technique is proposed to process the edge image for grouping the edge points into contours. The triangulation of the vertices located on inner and outer contours construct the search space for performing the snake model. To avoid the local minimum trapping, dynamic programming approach is used for finding the shortest path. Experimental

results show that we can obtain pretty good approximation for the heart chambers which are star-shaped and general cases by the proposed approaches.

Chapter 5

Finding the Mitral Annular Line

5.1 Introduction

Hitherto, we have focussed on region-based segmentation algorithms, proposed in chapter 3, and edge-based segmentatin algorithms, proposed in chapter 4, for echocardiographic image segmentation. We presented the good preforance of these four proposed algorithms for extracting the heart chambers from echocardiographic images within noisy. However, besides wall detection problem, another problem occurs when the left ventricle is segmented in the apical four-chamber echocardiogram view. In diastole, the left ventricle and left atrium become one chamber when the mitral valve opens fully. However, in systole the left ventricle and left atrium are separated by a mitral annular line. This line can be used as a reference to separate the two chambers in diastole. Thus, a convenient method to establish the mitral annular lines is needed toward designing an automatic method to calculate the left ventricle volume.

In this chapter, we present a nearly automatic method to establish the mitral annular lines from a 2D+1D precordial echocardiogram sequence. These images are preprocessed by the signal-adaptive maximun likelihood (SML) filter to remove speckle noise. We use the optical flow technique and 3-means algoritm to detect a set of points that could be on the mitral annulus. The mitral annular line connects a pair of such points. The problem to determine a sequence of mitral annular lines is modeled as a proclem that finding the shortest path in a

graph.

The remainder of this chapter is organized as follows. The proposed algorithm for finding mitral annular lines is described in Section 5.2. In Section 5.3 we present the experimental result obtained by the proposed algorithm. Discussions are given in Section 5.4.

5.2 Method

The proposed method uses the signal-adaptive maximum likelihood filter[50, 73], the optical flow computation[8, 36, 49, 52, 69], k-means algorithm[67] and shortest path algorithm[24]. The signal-adaptive maximum likelihood filter is for image preprocessing. To determine the mitral annular line sequence, the k-means algorithm is employed to determine a set of possible mitral annular points. Optical flow computation is then applied to estimate the velocities of the points. Finally, a weighted directed graph is established from these points and estimated velocities. The mitral annular line sequence is calculated by finding the shortest path in the graph.

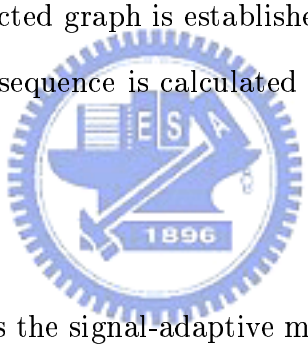

5.2.1 Preprocess

The preprocessing step employs the signal-adaptive maximum likelihood (SML) filter[50, 73] to remove the speckle noises. The SML filter abates noise and strengthens the signals from areas with similar intensities. The SML filter is now briefly described.

An image consists of low frequency and high frequency components. The low frequency component can be estimated using a local estimator. Given a $W \times W$ window around the pixel (k, l) in an image, the original (k, l) signal can be estimated using the maximum likelihood estimator $\hat{s}_{ML}(k, l)$ based on the observations in a $W \times W$ window. The original signal estimation at (k, l), denoted $\hat{s}(k, l)$, is obtained using

$$\hat{s}(k,l) = \hat{s}_{\mathrm{ML}}(k,l) + \beta(k,l)[x(k,l) - \hat{s}_{\mathrm{ML}}(k,l)]. \tag{5.1}$$

In Eq. (5.1), $x(k, l)$ is the intensity of the pixel (k, l). $\hat{s}_{ML}(k, l)$ is the maximum likelihood

estimation for the original signal at (k,l). $\beta(k,l)$ is a weighting factor that approximates the local SNR over the window. Using the multiplicative noise model, $\hat{s}_{ML}(k,l)$ and $\beta(k,l)$ are formulated as the following equations,

$$\hat{s}_{\mathrm{ML}}(k,l) = \frac{\sqrt{\pi}}{2}\sqrt{\frac{1}{N}\sum_{W} x^2(k-i,l-j)}, \tag{5.2}$$

and

$$\beta(k,l) = 1 - \left(\frac{4-\pi}{4}\right)\frac{Ew[x^2]}{Ew[(x-\hat{s}_{\mathrm{ML}})^2]}, \tag{5.3}$$

where $Ew[x^2] = \frac{1}{N}\sum_W x^2(i,j)$. The value of $\beta(k,l)$ ranges over [0,1]. If $\beta(k,l)$ is small, (k,l) is considered a noise point and its intensity is altered by the maximum likelihood estimation.

5.2.2 Computing the Mitral Annular Lines

In this step, a point that exists in the left ventricular chamber interior and separates the left and right attachments of mitral annular lines at all times in a cardiac cycle must be provided. There are four tasks in this step, namely, identifying the set of possible mitral annular points, estimating the velocities of the mitral annular points, establishing a weighted directed graph and finally computing the mitral annular lines.

Identify the Mitral Annular Points

The mitral annular points on fat and muscle demarcation have higher echogenecity. Thus, these mitral annular points will be in the brighter areas in the image. A 3-means algorithm is applied to divide the intensity into three clusters. The cluster, S, consisting of the highest intensity pixels contains the mitral annular points. Since a mitral annular line is formed by a pair of boundary points in S, only the boundary points are considered the possible mitral annular points in the later computation.

Estimate the Velocities

The velocities of these points are needed to determine the weights associated with edges in the graph. Because the true velocities are not available, the estimated velocities are calculated

using the optical flow technique. This method is briefly stated next. For details, please refer to [69].

Optical flow is a technique used to estimate the velocities of points from a pair of consecutive images. The velocities are estimated using the conservation and neighborhood information. The estimated velocities $U_{cc} = (u_{cc}, v_{cc})$ are computed using the conservation information. Errors exist between the estimated and true velocities. Assume that these errors have zero mean and are independent. A covariance matrix, S_{cc}, is used for the estimated velocity U_{cc}. The estimated velocities $\overline{U} = (\overline{u}, \overline{v})$ are obtained from the neighborhood information. The covariance matrix with the estimate is S_n. When we compute the mitral annular lines, we need the velocities of some image points to establish the weights of the edges in the graph G. We do not have the true velocities. The velocities are estimated using the optic flow technique from pair of consecutive images.

Optic flow is a technique to match the points between pairs of consecutive images. If we take the time between two images as a unit, then optic flow is used to estimate the velocity.

The optic flow estimation recovers the conservation information and propagates it using neighborhood information. The conservation information can be obtained using a correlation-based approach. Let I_1 and I_2 be two consecutive images. Assume that the image brightness is stationary with respect to time. For a point $p = (x, y)$ in I_1, the optic flow technique is used to determined the corresponding point p' in the next image as the follows. We first set up a $(2n+1)$ by $(2n+1)$ window W_p around the point $p = (x, y)$ and a $(2N+1)$ by $(2N+1)$ window W_s around (x, y) in I_2 as the search area. W_s must cover the location of p'. The error function is estimated using the sum of square differences (SSD), denoted $E_c(u, v)$, for every point in W_s as

$$E_c(u,v) = \sum_{i=-n}^{n} \sum_{j=-n}^{n} \left[I_1(x+i, y+j, t) - I_2(x+u+i, y+v+j, t+1) \right]^2, -N \leq u, v, \leq N.$$

The response distribution in velocity space is

$$R_c(u,v) = e^{-kE_c(u,v)},$$

where k is a constant close to zero (0.001). Having the response distribution function, the expected velocity $U_{cc} = (u_{cc}, v_{cc})$ is estimated using a weighted least squares approach. The estimate is given by

$$u_{cc} = \frac{\sum_{u=-N}^{N}\sum_{v=-N}^{N} R_c(u,v)u}{\sum_{u=-N}^{N}\sum_{v=-N}^{N} R_c(u,v)},$$

and

$$v_{cc} = \frac{\sum_{u=-N}^{N}\sum_{v=-N}^{N} R_c(u,v)v}{\sum_{u=-N}^{N}\sum_{v=-N}^{N} R_c(u,v)}.$$

There are errors between the estimated velocities and the true velocities. Assume that the errors have zero mean and are independent. The covariance matrix with the estimate given above is

$$S_{cc} = \begin{bmatrix} \frac{\sum_u\sum_v R_c(u,v)(u-u_{cc})^2}{\sum_u\sum_v R_c(u,v)} & \frac{\sum_u\sum_v R_c(u,v)(u-u_{cc})(v-v_{cc})}{\sum_u\sum_v R_c(u,v)} \\ \frac{\sum_u\sum_v R_c(u,v)(u-u_{cc})(v-v_{cc})}{\sum_u\sum_v R_c(u,v)} & \frac{\sum_u\sum_v R_c(u,v)(v-v_{cc})^2}{\sum_u\sum_v R_c(u,v)} \end{bmatrix}.$$

Since the conservation information is not complete, we need the neighborhood information to estimate the velocities of all the image points. For a given point $p = (x, y)$, assume that the velocities of the pixels in a $(2w+1) \times (2w+1)$ window, W_p, around (x, y) are known. We can treat these velocities as a measurement of the velocity of p. The estimated velocity of p, $\overline{U} = (\overline{u}, \overline{v})$ can be obtained based on the weighted least square as follows:

$$\overline{u} = \frac{\sum_u\sum_v R_n(u,v)u}{\sum_u\sum_v R_n(u,v)},$$

and

$$\overline{v} = \frac{\sum_u\sum_v R_n(u,v)v}{\sum_u\sum_v R_n(u,v)}.$$

The weight $R_n(u,v)$ is determined using a Gaussian mask centered at (u,v). The covariance matrix with the estimate is

$$S_n = \begin{bmatrix} \frac{\sum_u\sum_v R_n(u,v)(u-\overline{u})^2}{\sum_u\sum_v R_n(u,v)} & \frac{\sum_u\sum_v R_n(u,v)(u-\overline{u})(v-\overline{v})}{\sum_u\sum_v R_n(u,v)} \\ \frac{\sum_u\sum_v R_n(u,v)(u-\overline{u})(v-\overline{v})}{\sum_u\sum_v R_n(u,v)} & \frac{\sum_u\sum_v R_n(u,v)(v-\overline{v})^2}{\sum_u\sum_v R_n(u,v)} \end{bmatrix}.$$

The conservation and neighborhood errors are respectively

$$(U - U_{cc})^T S_{cc}^{-1} (U - U_{cc}) \tag{5.4}$$

and

$$(U - \overline{U})^T S_n^{-1} (U - \overline{U}). \tag{5.5}$$

By minimizing the sum of the conservation and neighborhood errors

$$\int\int [(U - U_{cc})^T S_{cc}^{-1} (U - U_{cc}) + (U - \overline{U})^T S_n^{-1} (U - \overline{U})], \tag{5.6}$$

the true velocity can be estimated. Minimizing Eq. (5.6) is carried out by applying an iteration method. The velocity of the $(n+1)$st iteration is calculated using

$$U^{n+1} = [S_{cc}^{-1} + S_n^{-1}][S_{cc}^{-1} U_{cc} + S_n^{-1} \overline{U}^n]. \tag{5.7}$$

The boundary condition is $U^0 = U_{cc}$. The iteration stops when the difference between the velocities of two successive iterations is smaller than a given threshold value.

Finding the Mitral Annular Lines

Let the image sequence be denoted I_i, $i = 1, \ldots, r$. Each I_i is preprocessed using the 3-means algorithm to identify those points that could be the mitral annular points. Let the user input a selected point denoted O so that a vertical line passing through O divides the point set into two subsets L_i and R_i. A mitral annular line is formed by a pair of points (p, q) that $p \in L_i$ and $q \in R_i$. Each line segment, $\overline{p_j, q_k}$, $p_j \in L_i$, $q_k \in R_i$ is a *candidate* for the mitral annular line.

Let v_{L_i} and v_{R_i} be the average velocities of the points in L_i and R_i. If $\overline{p_i, q_i}$ and $\overline{p_{i+1}, q_{i+1}}$ are the mitral annular lines in I_i and I_{i+1}, $|(\overrightarrow{p_i, p_{i+1}} - v_{L_i})| + |(\overrightarrow{q_i, q_{i+1}} - v_{R_i})|$ should be small. Based on this observation, a method to identify the mitral annular line sequence from I_1 to I_r was designed using the graph-search approach.

A weighted directed graph $G = (V, E)$ is constructed. V is the set of vertices that $V = \cup V_i, i = 1, \ldots, r$. $V_i = \{v_{(i,j)} | j = 1, \ldots, m_i\}$ where $v_{(i,j)}$ is the jth candidate for the mitral

annular line in I_i and m_i is the number of candidates in I_i. E is the set of directed edges $\{< v_{(i,j)}, v_{(i+1,k)} > | i = 1, \ldots, r-1, j = 1, \ldots, m_i, k = 1, \ldots, m_{i+1}\}$. There is a weight, $w_{(i,j,k)}$, associated with an edge $< v_{(i,j)}, v_{(i+1,k)} >$. Let $v_{(i,j)}$ represent a candidate $\overline{p_i, q_i}$ and $v_{(i+1,k)}$ represent a candidate $\overline{p_{(i+1)}, q_{(i+1)}}$. Given the velocities v_{L_i} and v_{R_i}, the weight $w_{(i,j,k)}$ is defined using Eq. (5.8).

$$w_{(i,j,k)} = |(\overrightarrow{p_i, p_{i+1}} - v_{L_i})| + |(\overrightarrow{q_i, q_{i+1}} - v_{R_i})|. \tag{5.8}$$

Suppose that $\overline{p_i, q_i}$, $i = 1, \ldots, r$, are the sequence of mitral annular lines in I_i. The sum of the weights w_i, $i = 1, \ldots, r-1$ should be the minimum. Thus, given the weighted graph G, the shortest path from a vertex in V_1 to a vertex in V_r corresponds to the mitral annular line sequence.

To implement the shortest path algorithm, there are two fields, $c_{(i,j)}$ and $f_{(i,j)}$, associated with each vertex $v_{(i,j)}$. $c_{(i,j)}$ maintains the least path cost from a vertex in V_1 to $v_{(i,j)}$. $f_{(i,j)}$ records the vertex in V_{i-1} on that path. The algorithm is presented in the following pseudo code.

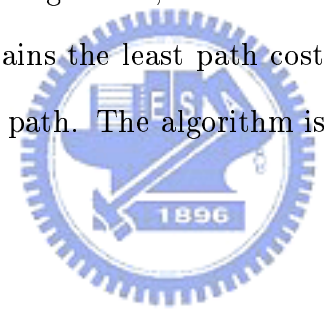

```
set v(1,j) = 0, j = 1, ..., m1;
set v(i,j) = a large number for all i ≠ 1, for all j;
for (i=2 to r) {
    for (j=1 to mi) {
        for (k = 1 to mi-1) {
            if (c(i,j) > w(i-1,k,j) + c(i-1,k)) {
                c(i,j) = w(i-1,k,j) + c(i-1,k);
                f(i,j) = v(i-1,k);
            }
        }
```

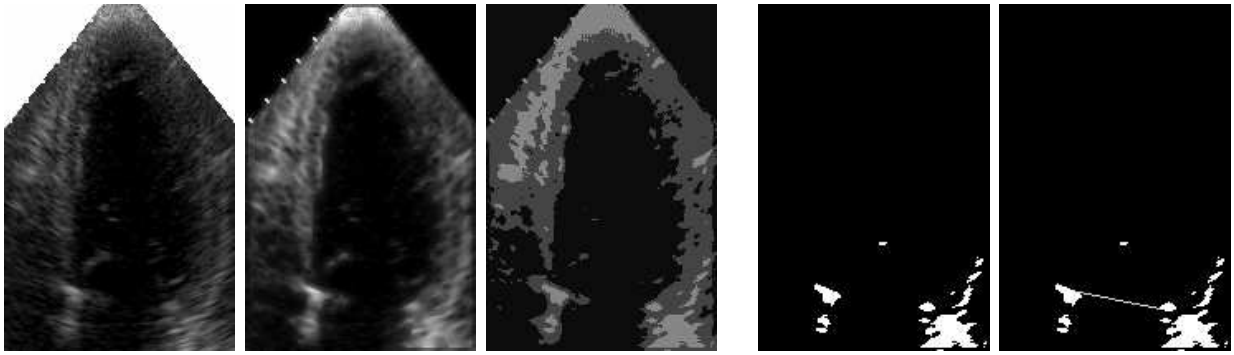

Figure 5.1: The images before (upper left) and after (upper middle) the SM filter application. The image after applying the 3-means clustering method is shown in the upper right most image. The lower left image shows the selected point O and the points in the highest intensity cluster. Only the boundary points are the possible mitral annular points. The lower right image shows the superimposed mitral annular line.

Table 5.1: Computation time required in each step. The time was obtained using an AMD Athlon (TM) XP 1500+ CPU.

SML Filtering	25 sec.
Optical flow computing	67 sec.
Shortest Path Computation	123 sec.

}

}

5.3 Experimental Results

The experimental results are presented in this section. The image resulting from the SM filter application is presented in Figure 5.1. The image after 3-means clustering is also shown in Figure5.1. The cluster that has the largest intensity contains the possible mitral annular points. Only the points below the selected point O are considered to be the possible mitral annular points.

Figure 5.2 shows a sequence of identified mitral annular lines obtained using the proposed method. The computing time for processing a sequence of 20 images is shown in Table 5.1. The computation time was recorded using an AMD Athlon (TM) XP 1500+ personal computer.

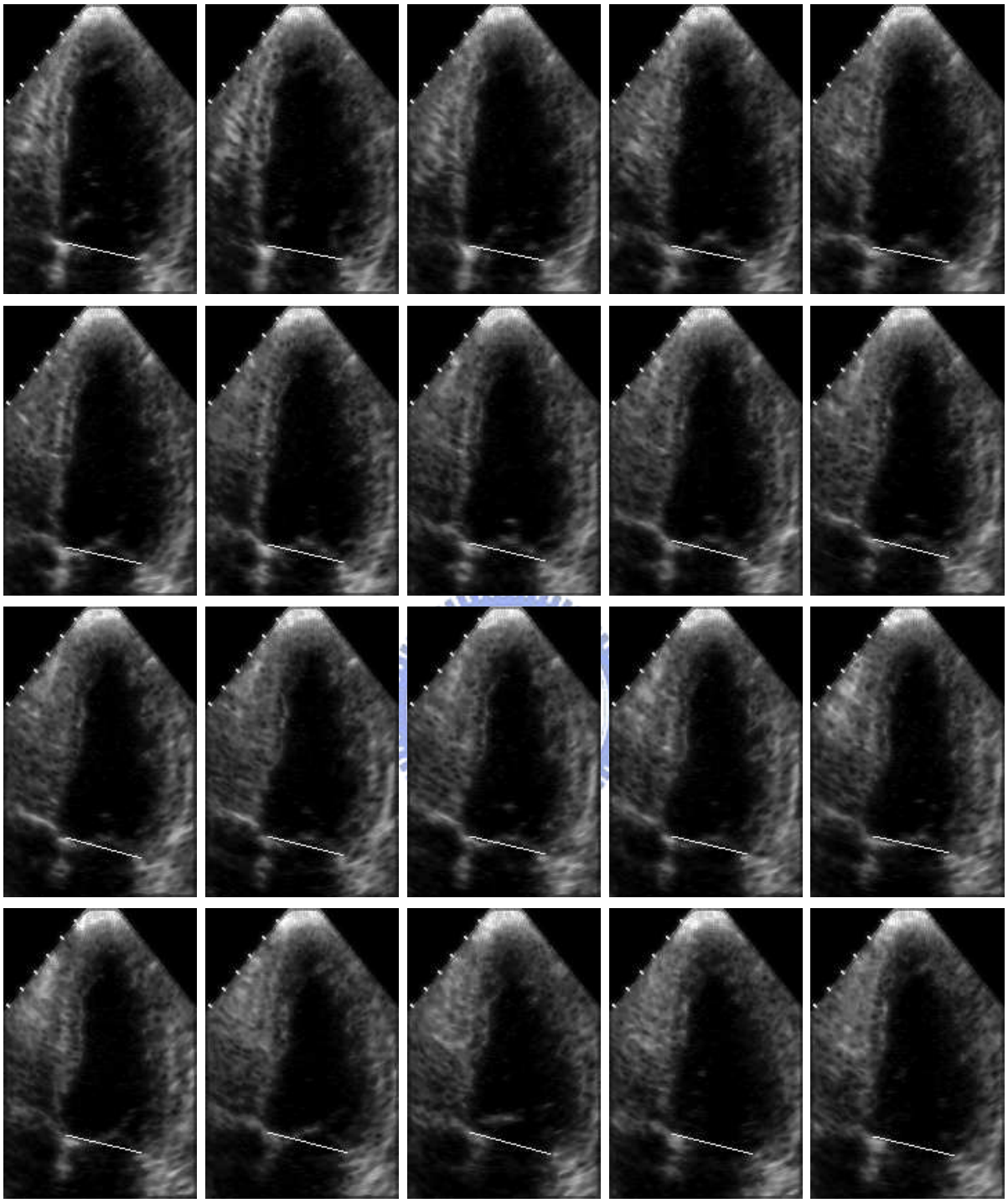

Figure 5.2: Sequential precordial echocardiographic images in long axis view of an adult healthy volunteer within a cardiac cycle. The white line separating the left ventricle and left atrium is the mitral annular line created by the proposed method.

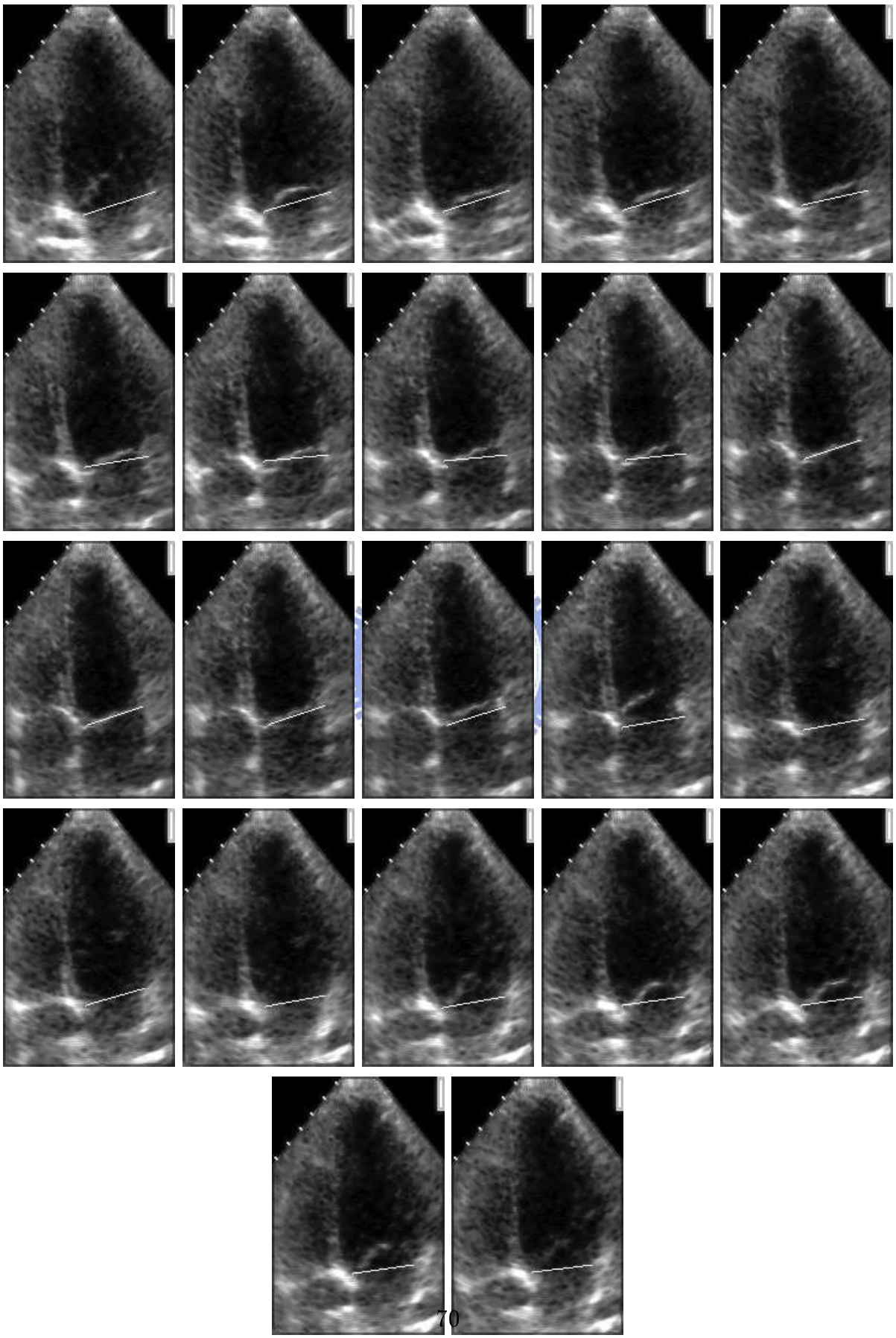

Figure 5.3: A result obtained using the proposed method, case 2.

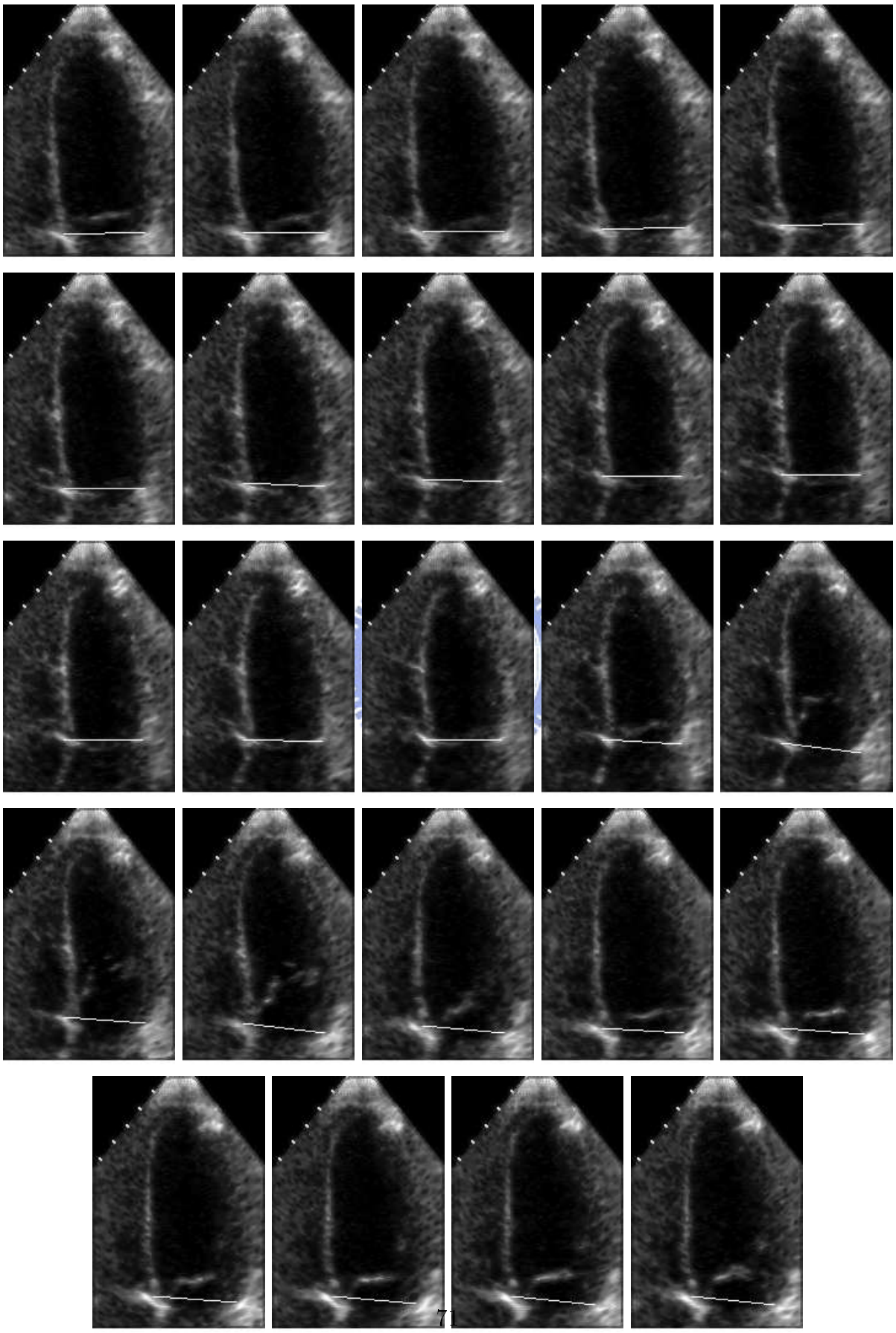

Figure 5.4: A result obtained using the proposed method, case 3.

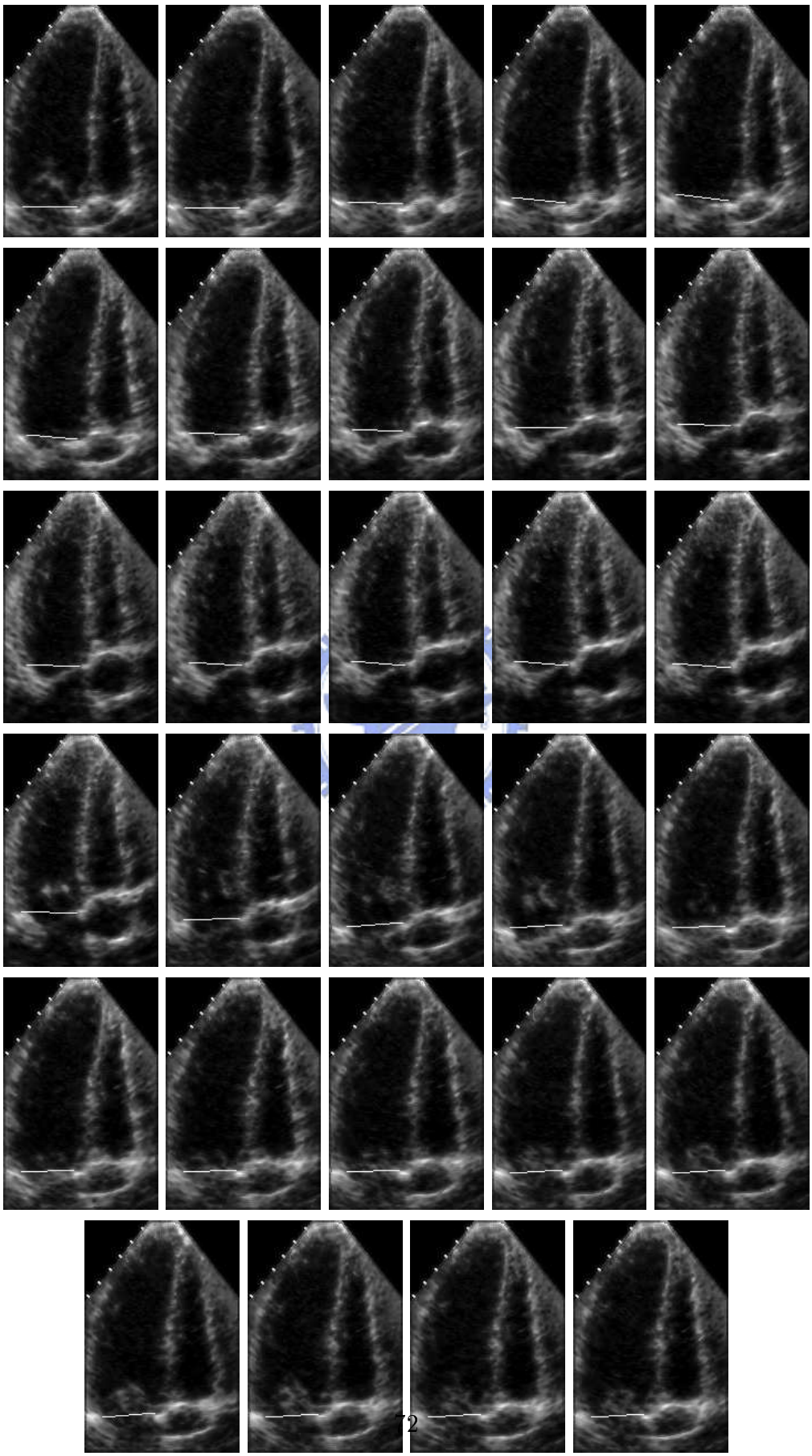

Figure 5.5: A result obtained using the proposed method, case 4.

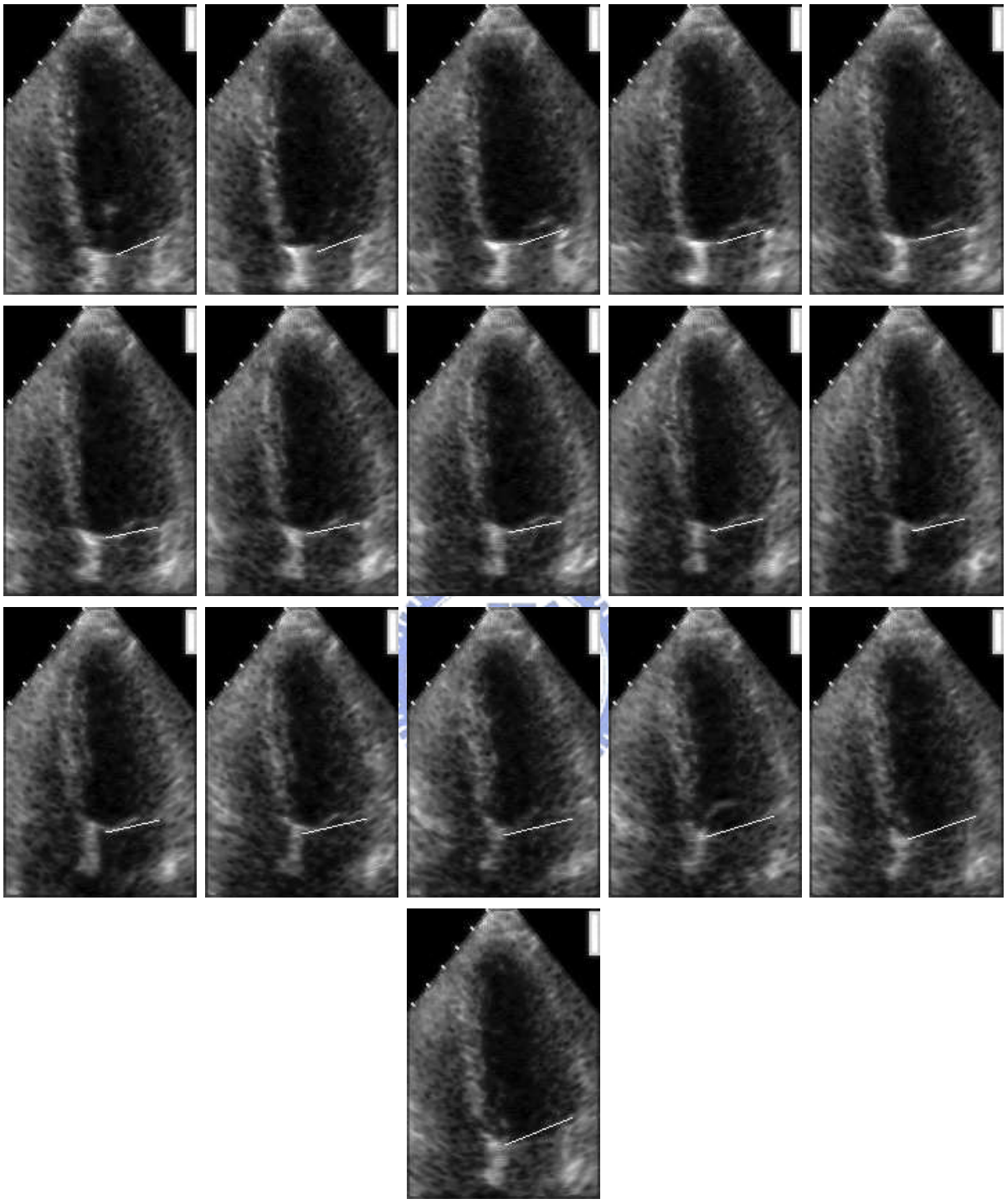

Figure 5.6: A result obtained using the proposed method, case 5.

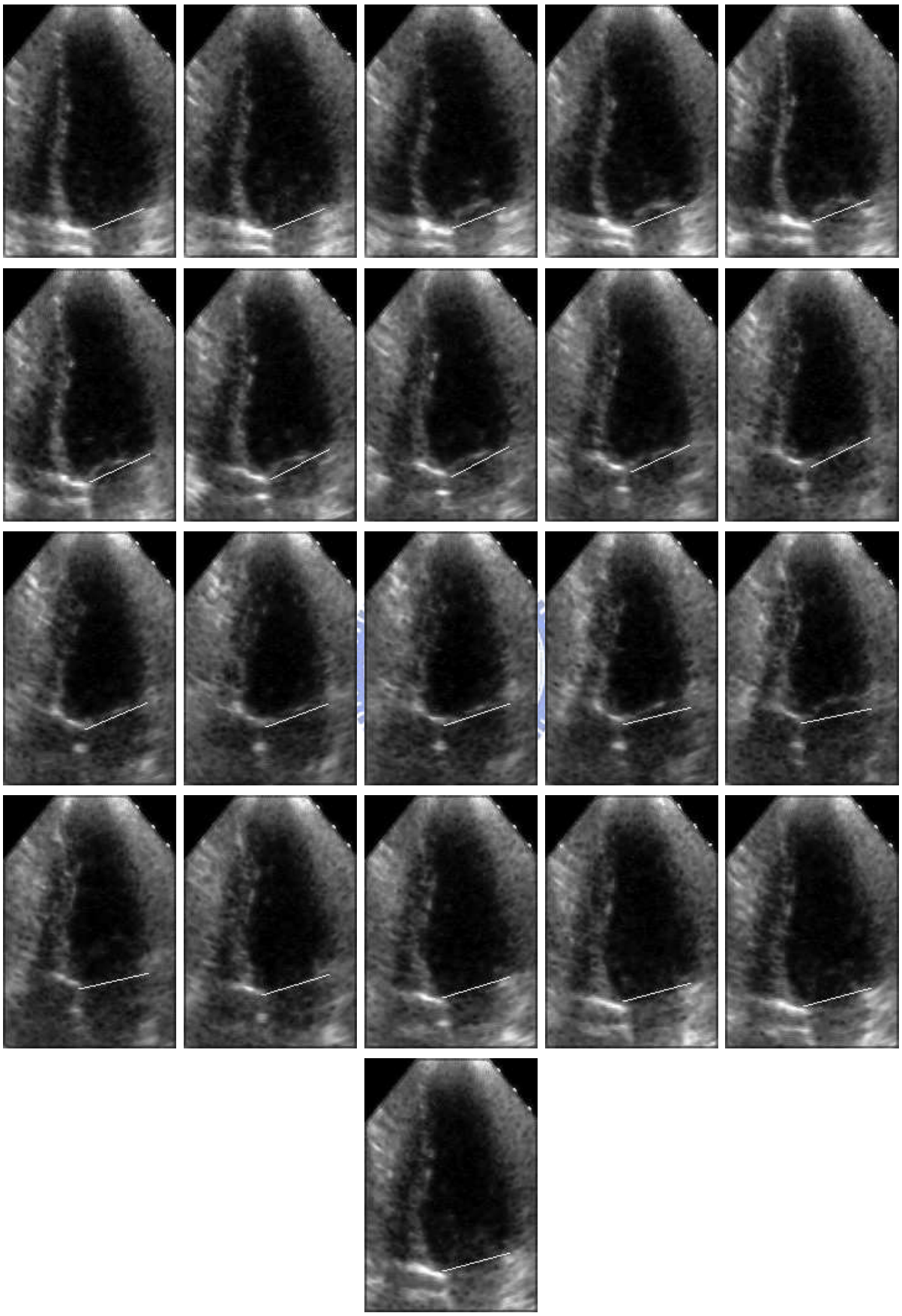

Figure 5.7: A result obtained using the proposed method, case 6.

Table 5.2: The error distribution for the 148 images.

Error	Number of Images
0.01	33
0.02	24
0.03	25
0.04	18
0.05	16
0.06	16
0.07	7
0.08	3
0.09	4
0.1	2

The computation time required by the first and the second step depends on the image size. The image size was 140 by 210 in our experiment. The computation time required for Step 3 depends on the number of mitral annular line candidates. This was the most time consuming step. The time complexity for the algorithm in Step 3 is $O(r \cdot m^2)$ where m is the number of candidates in each image and r is the number of images in the sequence. The run time was recorded when the number of candidates was 4225, i.e., we restricted the number of candidates for mitral annular points to 65 points on each side. These 65 points are below the point O and they are the 65 closest points to O horizontally.

To test the accuracy of the proposed method, the method was applied to 7 mitral annular lines sequence cases. These 7 cases were chosen because the junctions between the left atrium and left ventricle were anatomically obvious. The endocardial wall of the left ventricle was traced and the volume of the heart chamber was calculated based on the mitral annular lines obtained using the computer and by a physician. There were 7 cases consisting of 148 images. The volume was obtained using the proposed method, V_c, and a physician tracing V_p. We computed the difference $d = V_c - V_p$. The error was evaluated using $|d|/V_p$. Our results show that the averaged error was 0.03. Table 1 shows the error distribution for the 148 images.

5.4 Discussions

In this chapter, a nearly automatic method for calculating the mitral annular lines from a 2D+1D precordial echocardiogram four-chamber view was presented. We applied the proposed method to 7 mitral annular line sequence cases. The proposed method needs only a physician to provide a point in the left ventricular chamber. The average error was 3% which is clinically acceptable. The proposed method saves much clinician time, allowing a shift from machine to patient care.

Chapter 6

Conclusions

In this dissertation, we have proposed two region-based segmentation algorithms and two edge-based segmentation algorithms for echocardiographic images analysis. The first proposed algorithm for region-based segmentation scheme is fuzzy Hopfield neural network with fixed weight approach. This approach incorporates the global gray-level information to construct the fuzzy Hopfield neural network. According to our experiments, the performance of the proposed approach is much better than the hard c-means, fuzzy c-means, and competitive Hopfield neural network methods. A new approach using α-shape points is another proposed algorithm based on edge-detection category. In our experimental results, there were more than one thousand α-connected components for an α. Most of them contained only a very small number of points. The proposed algorithm worked well when the region of interests were sufficiently large. The first proposed algorithm for edge-based segmentation scheme is finding the shortest path in directed graph. We circularly spread the image first and then map it to a directed graph. To avoid the local minimum trapping, dynamic programming approach is used for finding the shortest path. The other proposed approach for edge-based segmentation algorithm is suitable for non circular like boundary. Instead of spreading the image, we incorporated an α-contour approach based on α-shape technique to construct the search space. From the implemented results of these two algorithms, we can obtain pretty good approaximation for cardiac boundary extraction.

In additional, we also propose a new approach for extracting mitral annular lines for echocardiographic images. A nearly automatic method for calculating the mitral annular lines from a 2D+1D precordial echocardiogram four-chamber view was presented. The proposed method needs only a physician to provide a point in the left ventricular chamber. The average error was 3% which is clinically acceptable. The proposed method saves much clinician time, allowing a shift from machine to patient care.

One important fact in the development of segmentation techniques is that no general theory exists, and *ad hoc* solutions are traditionally proposed. Although some initial attempts in the direction of a unified theory were reported, this problem is far from being solved, and none of the developed techniques is generally applicable. Given a particular application, finding the appropriate segmentation algorithm is still a problem.

In this disertation, we presented methods dealing different cases. Each method needs very few user interfaces and is almost automatic. The future work will be in two directions. The first is that since 3D echocardiogram is available, it is a challenge task to design reliable algorithms to deal with 3D case. The second is to develop GUI systems that help physicain to easily use the developed methods.

Bibliography

[1] R. Adams and L. Bischof, "Seeded Region Growing," IEEE Transactions on Pattern Analysis and Machine Intelligence, Vol. 16, No. 6, pp. 641-647, June 1994.

[2] M. Allen, Echocardiography- 2nd edition. Philadelphia, New York, Lippincott, Chapter 9, 1999.

[3] American Heart Association, American Heart Association 1999 Statistics [Online], Available: http://www.americanheart.org/.

[4] M. Basu, "Gaussian-Based Edge-Detection Methods - A survey," IEEE Transactions on Systems, Man, and Cybernetics - Part C: Applications and Reviews, Vol. 32, No. 3, pp. 252-260, 2002.

[5] D. Baukerroui, O. Basset, A. Baskurt, and G. Gimenez, "A Multiparametric and Multiresolution Segmentation Algorithm of 3-D Ultrasonic Data," IEEE Transactions on Ultrasonics, Ferroelectrics and Frequency Control, Vol. 48, Issue: 1, pp. 64-77, January 2001.

[6] J. C. Bezdek, "Cluster Validity with Fuzzy Sets," Jounral of Cybernetics, Vol. 3, pp. 58-73, 1974.

[7] B. Bijnens, M. van Hamme, J. Vandekerckhove, M. C. Herregods, J. Nuyts, P. Suetens, and F. van de Werf, "Segmentation of Echocardiographic Images Using Classification in

the Radiofrequency Feature Space," Computers in Cardiology, pp. 733-736, September 1995.

[8] A. D. Bimbo, P. Nesi, and J. L. Sanz, "Optical Flow Computation Using Extended Constraints," IEEE Transactions on Image Processing, Vol. 5, No. 5, pp. 720-739, May 1996.

[9] W. E. Blanz and S. L. Gish, "A connectionist classifier architecture applied to image segmentation," Proceedings, 10th International Conference on Pattern Recognition, pp. 272-277, June 1990.

[10] J. Bosch, G. van Burken, S. Schukking, R. Wolff, A. van de Goor, and J. Reiber, "Real-time Frame-to-frame Automatic Contour Detection on Echocardiogram," Computer in Cardiology, pp. 29-32, 1994.

[11] J. G. Bosch, S. C. Mitchell, B. P. Lelieveldt, F. Nijland, O. Kamp, M. Sonka, and J. H. Reiber, "Automatic Segmentation of Echocardiographic Sequences by Active Appearance Motion Models," IEEE Transactions on Medical Imaging, Vol. 21, No. 11, pp. 1374-1383, November 2002.

[12] A. Bosnjak, V. Burdin, V. Torrealba, G. Montilla, B. Solaiman, and C. Roux, "3D Modeling and Parameterization of The Left Ventricle in Echocardiographic Images Using Deformable Superquadrics," Comouters in Cardiology, Vol. 28, pp. 101-104, 2001.

[13] A. E. Boudraa, J. J. Mallet, J. E. Besson, S. E. Bauyoucef, and J. Champier, "Left Ventricle Automated Detection Method in Gated Isotopic Ventriculography Using Fuzzy Clustering," IEEE Transactions on Medical Imaging, Vol. 12, No. 3, pp. 451-465, September 1993.

[14] C. W. Chen, J. Luo, K. J. Parker, and T. S. Huang, "A Knowledge-Based Approach to Volumetric Medical Image Segmentation," Proceedings, IEEE International Conference on Image Processing, Vol. 3, pp. 493-497, Nonember 1994.

[15] C. W. Chen, J. Luo, and K. J. Parker, "Image Segmentation via Adaptive K-Mean Clustering and Knowledge-Based Morphological Operations with Biomedical Applications," IEEE Transactions on Image Processing, Vol.7, No. 12, December 1998.

[16] C. T. Chen, E. C. Tsao, and W. C. Lin, "Medical Image Segmentation by a Constraint Satisfaction Neural Network," IEEE Transactions on Nuclear Science, Vol. 38, No. 2, pp. 678-686, April 1991.

[17] K. S. Cheng, J. S. Lin, and C. W. Mao, "The Application of Competitive Hopfield Neural Network to Medical Image Segmentation," IEEE Transactions on Medical Imaging, Vol. 15, No. 4, pp. 560-567, August 1996.

[18] M. M. Choy and J. S. Jin, "Improving Border Identification in Two-dimensional Echocardiograms Using Temporal Information," Proceedings of 18th Annual International Conference of the Enhineering in Medicine and Bioligy Society, Vol. 2, 1996, pp. 879-880, October 1996.

[19] C. H. Chu, E. J. Delp, and A. J. Buda, "Detecting Left Venreicular Endocardial and Epicardial Boundaries by Digital Two-Dimensional Echocardiograpgy," IEEE Transactions on Medical Imaging, Vol. 7, No. 2, pp.81-90, June 1988.

[20] C. H. Chu, and E. J. Delp, "Detecting Heart Wall Boundaries by Tracking Features in an Echocardiogram Sequence," Computer in Cardiology, pp. 117-120, 1988.

[21] P.C. Chung, C.T. Tsai, E.L. Chen and Y.N. Sun, "Polygonal Approximation Using a Competitive Hopfield Neural Network," Pattern Recognition, Vol. 27, No. 11, pp. 1505-1512, 1994.

[22] K.L. Clarkson, K. Mehlhorn, and R. Seidel, "Four results on randomized incremental Constructions," Computer Geometry: Theory and Applications, pp. 185-121, 1993.

[23] G. Coppini, R. Poli, and G. Valli, "Recovery of the 3-D Shape of the Left Ventricle from Echocardiographic Images," IEEE Transactions on Medical Imaging, Vol. 14, No. 2, pp. 301-317, 1995.

[24] T. H. Cormen, C. E. Leiserson, R. L. Rivest, and Clifford Stein, Introduction to Algorithms, M.I.T. press. 1989.

[25] G. Deng and L. W. Cahill, "An Adaptive Gaussian Filter for Noise Reduction and Edge Detection," IEEE Conference on Nuclear Science Symposium and Medical Imaging Conference, Vol. 3, pp. 1615-1619, November 1993.

[26] A. P. Dhawan and L. Arata, "Segmentation of Medical Images Through Competitive Learnings," IEEE International Conference on Neural Networks, Vol. 3, pp. 1277-1282, April 1993.

[27] H. Edelsbrunner and P. Ernest, "Three-dimensional alpha shapes," ACM. Transactions on Graphics, Vol. 13, No. 1, pp. 43-72, 1994.

[28] A.F. Frangi, W.J. Niessen, and M.A. Viergever, "Three-Dimensional Modeling for Function Analysis of Cardiac Images: A Review," IEEE Transactions on Medical Imaging, Vol. 20, No. 1, pp. 2-25, 2001.

[29] K.S. Fu and J.K. Mui, "A Survey on Image Segmentation," Pattern Recognition, Vol. 13, pp. 3-16, 1981.

[30] R. C. Gonzalez and R. E. Woods, Digital Image Processing. Reading, MA: Addison-Wesley, 1992.

[31] J. 3rd Gorcsan, S. Morita, W. A. Mandarino, L. G. Deneault, A. Kawai, R. L. Kormos, B. P. Griffith, and M. R. Pinsky, "Two dimensional echocardiographic automated border detection accurately reflects changes in left ventricular volume," Journal of the American Society of Echocardiography, Vol.6, pp.482-489, 1993.

[32] G. Hamarneh, and T. Gustavsson, "Combining Snake and Active Shape Models for Segmentatin the Human Left Ventricle in Echocardiographic Images," Computers in Cardiology, Vol. 27, pp. 115-118, 2000.

[33] X. Hang, N. L. Greenberg, and J. D. Thomas, "A Geometric Deformable Model for Echocardiographic Image Segmentation," Computers in Cardiology Vol. 29, pp. 77-80, September 2002.

[34] R. Haralick and Y. T. Liow, "Survey: Image Segmentation Techniques," Computer Vision Graphics, Image Processing, Vol. 29, pp. 100-132, 1985.

[35] R. M. Haralick, S. R. Sternberg, and X. Zhuang, "Image Analysis Using Mathematical Morphology," IEEE Transactions on Pattern Analysis and Machine Intelligence, Vol. PAMI-9, No. 4, pp. 532-550, July 1987.

[36] B. K. Horn and B. G. Schunck, "Determining Optical Flow," Artificial Intelligence, vol. 17, pp. 185-203, 1981.

[37] S. L. Horowitz and T. Pavlidis, "Picture segmentation by a directed splite-and-merge procedure," Proceedings, 2nd International Joint Conference on Pattern Recognition, pp. 424-433, 1974.

[38] E. Horowitz, S. Sahni, and S. Anderson-Freed, Fundamentals of Data Structure in C. Computer Science Press, New York, pp.239-247, 1993.

[39] N. Ikonomakis, K.N. Plataniotis, M. Zervakis, and A.N. Venetsanopoulos, "Region Growing and Region Merging Image Segmentation," Digital Signal Processing Proceedings, Vol. 1, pp. 2-4, July 1997.

[40] M. Kass, A. Witkin and D. Terzopoulos, "Snakes: Active Contour Models," Proceedings, 1st International Conference on Computer Vision, pp. 259-269, 1987.

[41] J. W. Klingler, C. L. Vaughan, T. D. Fraker, and L. T. Andrews, "Segmentation of Echocardiographic Images Using Mathematical Morphology," IEEE Transactions on Biomedical Engineering, Vol. 35, Issue. 11, pp. 925-934, November 1988.

[42] M. Kobashi and L. G. Shapiro, "Knowledge-based organ identification from CT images," Pattern Recognition, Vol. 28, No. 4, pp. 475-491, 1995.

[43] K. K. Ma and H. Y. Wang, "Region-Based Nonparametric Optical Flow Segmentation With Pre-Clustering and Post-Clustering," IEEE International Conference on Multimedia and Expo, Vol. 2, pp. 201-204, August 2002.

[44] J. S. Lin, K. S. Cheng, and C. W. Mao, "A Fuzzy Hopfield Neural Network for Medical Image Segmentation," IEEE Transactions on Nuclear Science, Vol. 43, No. 4, pp. 2389-2398, August 1996.

[45] J. S. Lin, K. S. Cheng, and C. W. Mao, "A Modified Hopfield Neural Network with Fuzzy C-Means Technique for Multispectral MR Image Segmentation," Proceedings of 3rd IEEE International Conference on Image Processing, Vol. 1, pp. 327-330, September 1996.

[46] R. Lin, S. Y. Chen, V. Mor-Avi, J. Bednarz, C. T. Chen, and R. M. Lang, "Three-Dimensional Reconstruction of the LV Endocardial Surfaces from Echocardiographic Images Using Deformable Shell Models," Computers in Cardiology, pp.697-700, 1996.

[47] W. C. Lin, E. C. Tsao, and C. T. Chen, "Constrain Satisfaction Neural Networks for Image Segmentation," Pattern Recognition, Vol. 25, No.7, pp. 679-693, 1992.

[48] P. Linares, V. Torrealba, G. Montilla, A. Bosnjak, C. Jimenez, and V. Barrios, "Deformable Model Application on Segmentation in 3-D Echocardiography," Computers in Cardiology, pp. 413-416, September1996.

[49] G. Mailloux, A. Bleau, M. Bertrand, and R. Petitclerc, "Computer Analysis of Heart Motion from Two-dimensional Echocardiograms," IEEE Transactions on Biomedical Engineering, vol. BME-34, pp. 356-364, May 1987.

[50] S. Malassiotis and M. Strintzis, "Tracking the Left Ventricle in Echocardiographic Images by Learning Heart Dynamics," IEEE Transactions on Medical Imaging, vol. 18, Issue 3, pp. 282-290, Mar. 1999.

[51] D. Marr and E. Hildreth, "Theory of Edge detection," Proceedings, Royal Soc. London. Vol. B207, pp. 187-217, 1980.

[52] I. Mikic, S. Krucinski, and J. Thomas, "Segmentation and Tracking in Echocardiographic Sequences: Active Contours Guided by Optical Flow Estimates," IEEE Transactions on Medical Imaging, vol. 17, Issue 2, pp.274-284, 1998.

[53] V. Mor-Avi, P. Vignon, R. Koch, L. Weinert, K. T. Spencer, and R. M. Lang, "Segmental analysis of Color Kinesis images: New method for quantitative assessment of left ventricular contraction and relaxation," Circulation Vol. 95, pp. 2082-2097, 1997.

[54] V. Mor-Avi, S. Y. Chen, R. Koch, D. Berger, J. Bednarz, K. Robinson, S. G. Shroff, and R. M. Lang, "Three-dimensional dynamic reconstruction of the left ventricular endocardial surface using acoustic quantification," Journal of American Society of Echocardiography, Vol. 9, p.3777(Abstract), 1996.

[55] M. Mulet-Parada and J. Noble, "Intensity-invariant 2D + T Acoustic Boundary Detection," 1998 Workshop on Biomedical Image Analysis, pp. 133-142, June 1998.

[56] W. Ohyama, T. Wakabayashi, F. Kimura, S. Tsuruoka, and K. Sekioka, "Automatic Left Ventricle Endocardium Detection in Echocardiograms Based on Ternary Thresholding Method," 15th International Conference on Pattern Recognition, Vol. 4, pp. 320-323, 2000.

[57] T. Ono and K. Ogawa, "Image Segmentation Using Circularly Spread MR Images," Nuclear Science Symposium and Midical Imaging Conference Record,Vol. 3, pp. 1493-1496, October 1995.

[58] N.R. Pal and S.K. Pal, "A Review on Image Segmentation Techniques," Pattern Recognition, Vol. 26, pp. 1277-1294, 1993.

[59] N. Paragios, "A Level Set Approach for Shape-Driven Segmentation and Tracking of the Left Ventricle," IEEE Transactions on Medical Imaging, Vol. 22, No.6, pp. 773-776, 2003.

[60] L. Piccoli, A. Dahmer, J. Scharcanski, and P. O. A. Navaux, "Fetal Echocardiographic Image Segmentation Using Neural Networks," International Conference on Image Processing and Its Applications, Pub No. 465, Vol. 2, pp. 507-511, July 1999.

[61] R. Poli, G. Coppini, R. Nobili, and G. Valli, "LV Shape Recovery From Echocardiographic Images by Means of Computer Vision Techniques and Neural Networks," Computer in Cardiology, pp. 117-120, 1991.

[62] F. P. Preparata and M. I. Shamos, Computational Geometry: An Introduction, Springer-Verlag Press, New York, 1985.

[63] R. J. Qian and T. S. Huang, "Optimal Edge Detection in Two-Dimensional Images," IEEE Transactions on Image Processing, Vol. 5, No. 7, pp.1215-1220, July 1996.

[64] J. Randall, L. Guan, X. Zhang, and W. Li, "The Hierarchical Cluster Model for Image Region Segmentation," International Conference on Multimedia and Expo, Vol. 1, pp. 693-693, August 2002.

[65] S. Ranganath, "Contour Extracion from Cardiac MRI Studies Using Snakes," IEEE Transactions on Medical Imaging, Vol. 14, No. 2, pp. 328-338, 1995.

[66] A. Salvador, Y. Maingourd, S. Fu, and J. F. Lerallut, "Optimization of An Edge Detection Algorithm for Echocardiographic Images," Proceedings of the 25th Annual International Conference of the Engineering in Medicne and Biology, pp. 1188-1191 ,September 2003.

[67] S. Z. Selim and M.A. Ismail, "K-Means-Type Algorithm: A Generalized Convergence Theorem and Characterization of Local Optimality," IEEE Transactions on Pattern Analysis and Machine Intellegence, Vol. 6, No. 1, pp. 81-86, January 1984.

[68] J. Shen and S. Castan, "Toward the Unification of Band-Limited Derivative Operators for Edge Detection," Signal Process, Vol. 34, pp. 321-343, 1986.

[69] A. Singh, Optic Flow Computation: A Unified perspective, IEEE Computer Society Press, Los Alamitos, CA, 1991.

[70] D. J. Skorton, S. M. Collins, E. Garcia, E. A. Geiser, W. Hillard, W. Koppes, D. Linker, and G. Schwartz, "Digital signal and image processing in echocardiography," American Heart Journal, Vol. 1, pp.1266-1283, 1985.

[71] L. H. Staib and J. S. Duncan, "Left Ventricular Analysis from Cardiac Images Using Deformable Models," Computers in Cardiology, pp. 427-430, September 1988.

[72] L. H. Staib and J. S. Duncan, "Boundary finding with parametrically deformable models," IEEE Transactions on Pattern Analysis and Machine Intelligence, Vol. 14, pp. 1061-1075, 1992.

[73] M. Strintzis, X. Magnisalis, C. Kotropoulos, I. Pitas, and N. Maglaveras, "Maximum Likelihood Signal Adaptive Filtering of Speckle in Ultrasound B-mode Images," IEEE Engineering Medicine Biology Society Conference, pp 1870-1871, 1992.

[74] L. Sui, F. H. Sheehan, and R. M. Haralick, "Automated Left Ventricle Boundary Delineation in Left Ventriculograms," Computers in Cardiology, Vol.27, pp.5-8, 2000.

[75] J. S. Suri, R. M. Haralick, and F. H. Sheehan, "Accurate Left Ventricle Apex Position and Boundary Estimation from Noisy Ventriculograms," Computers in Cardiology, pp. 257-260, 1996.

[76] H. D. Tagare, "Deformable 2-D Template Matching Using Orthogonal Curves," IEEE Transactions on Medical Imaging, Vol. 16, No. 1, pp. 108-117, February 1997.

[77] C. Vuille and A. E. Weyman, "Left Ventricle I: General considerations, assessment of chamber size and function," in *Principles and Practice of Echocardiography*, 2nd ed, A. E. Weyman, Ed. Philadelphia, PA: Lea and Febiger, 1994.

[78] S. Y. Wan and W. E. Higgins, "Symmetric Region Growing," IEEE Transactions on Image Processing, Vol. 12, No. 9, pp. 1007-1015, 2003.

[79] M. Sussner, M. Budil, T. Strohmer, M. Greher, G. Porenta, and T. Binder, "Contour Detection using Artificial Neural Network Pre-segmentation," Computers in Cardiology, pp. 737-740, 1995.

[80] Z. Xu, Q. Xia, and J. Chen, "The Performances of The Laplacian of Binomial Distribution and The discrete Laplacian of Gaussian Edge Detection Operators," Intelligent Systems for the 21st Century'., IEEE International Conference on Systems, Man and Cybernetics, Vol. 1, pp. 673-678, October 1995.

[81] X. Ye, J. A. Noble, and D. Atkinson, "3-D Freehand Echocardiography for Automatic Left Ventricle Reconstruction and Analysis Based on Mutiple Acoustic Windows," IEEE Transactions on Medical Imaging, Vol. 21, No. 9, pp. 1051-1058, September 2002.

[82] A. Yezzi, S. Kichenassamy, A. Kumar, P. Olver and A. Tannenbaum, "A Geometric Snake Model for Segmentation of Medical Imagery," IEEE Transactions on Medical Imaging, Vol. 16, No. 2, pp. 199-209, 1997.

[83] M. Zhang, L. O. Hall, and D. B. Goldgof, "A Generic Knowledge-Guided Image Segmentation and Labeling System Using Fuzzy Clustering Algorithms," IEEE Transactions on System, Man, and Cybernetics - Part B: Cybernetics, Vol. 32, No.5, October 2002.

[84] Y. Zhu and Z. Yan, "Computerized Tumor Boundary Detection Using a Hopfield Neural Network," IEEE Transactions on Medical Imaging, Vol. 16, No. 1, pp. 55-67, February 1997.

Vita

Mr. Chwen-Liang Chang received the B.S. degree in computer and information science from Chung-Chen Institute of Technology, Taiwan, R.O.C., in 1988. He is currently working toward the Ph.D. degree in the Department of Computer and Information Science, National Chiao-Tung University. His research interests include image processing, medical imaging, and neural network.